http://go.asme.org/HPVC

(Form 6)

Vehicle Description Form

Updated 12/3/13

Human Powered Vehicle Challenge

Competition Location: Orlando, Florida

Competition Date: April 11-13, 2014

This required document for all teams is to be incorporated in to your Design Report. Please Observe Your Due Dates; see the ASME HPVC for due dates.

Vehicle Description

School name: Rose-Hulman Institute of Technology
Vehicle name: Namazu
Vehicle number 1

Vehicle configuration

Upright	______	Semi-recumbent	✓
Prone	______	Other (specify)	______

Frame material 4130 Steel
Fairing material(s) Carbon Fiber, Kevlar
Number of wheels 3

Vehicle Dimensions *(please use in, in^3, lbf)*

Length	95 in	Width	31 in
Height	44 in	Wheelbase	38 in

Weight Distribution Front 60lbf Rear 30lbf Total Weight 90lbf
Wheel Size Front 20in (406) Rear 20in (406)
Frontal area 794 in^2
Steering Front ✓ Rear ✓
Braking Front Dual Rear ______ Both ______
Estimated Cd 0.19

Vehicle history (e.g., has it competed before? where? when?)

The vehicle has not competed before (but will be competing at HPVC West).

Rose-Hulman Institute of Technology

2014 ASME East Coast HPV Challenge

ROSE-HULMAN
HUMAN POWERED VEHICLE TEAM

Presents

Vehicle #1

Team Officers

Ben Griffith, President
griffibp@rose-hulman.edu
Garrett Meyer, Secretary
meyerg@rose-hulman.edu
Patrick Woolfenden, Vice President
Louis Vaught, Treasurer
Melissa Murray, Public Relations
Matt Skorina, Archivist

Team Advisors

Dr. Michael Moorhead
Associate Professor of Mechanical Engineering
moorhead@rose-hulman.edu
Dr. John McSweeney
Assistant Professor of Mathematics
mcsweene@rose-hulman.edu

Team Members

Josh Bertsche
Luke Brokl
Simon Burns
Ethan Cating
Elena Chong
Harrison Coons
Zeke DeSantis
Jeff Dovalovsky
Mitch Florence
Homa Hariri
Crystal Hurtle
Will Klausler
Drew Miner
Drew Robertson
Claire Stark
Travis Tatlock
Tyler Whitehouse

For more information, visit the team website at:
hpvt.rose-hulman.edu

Four-View Drawing

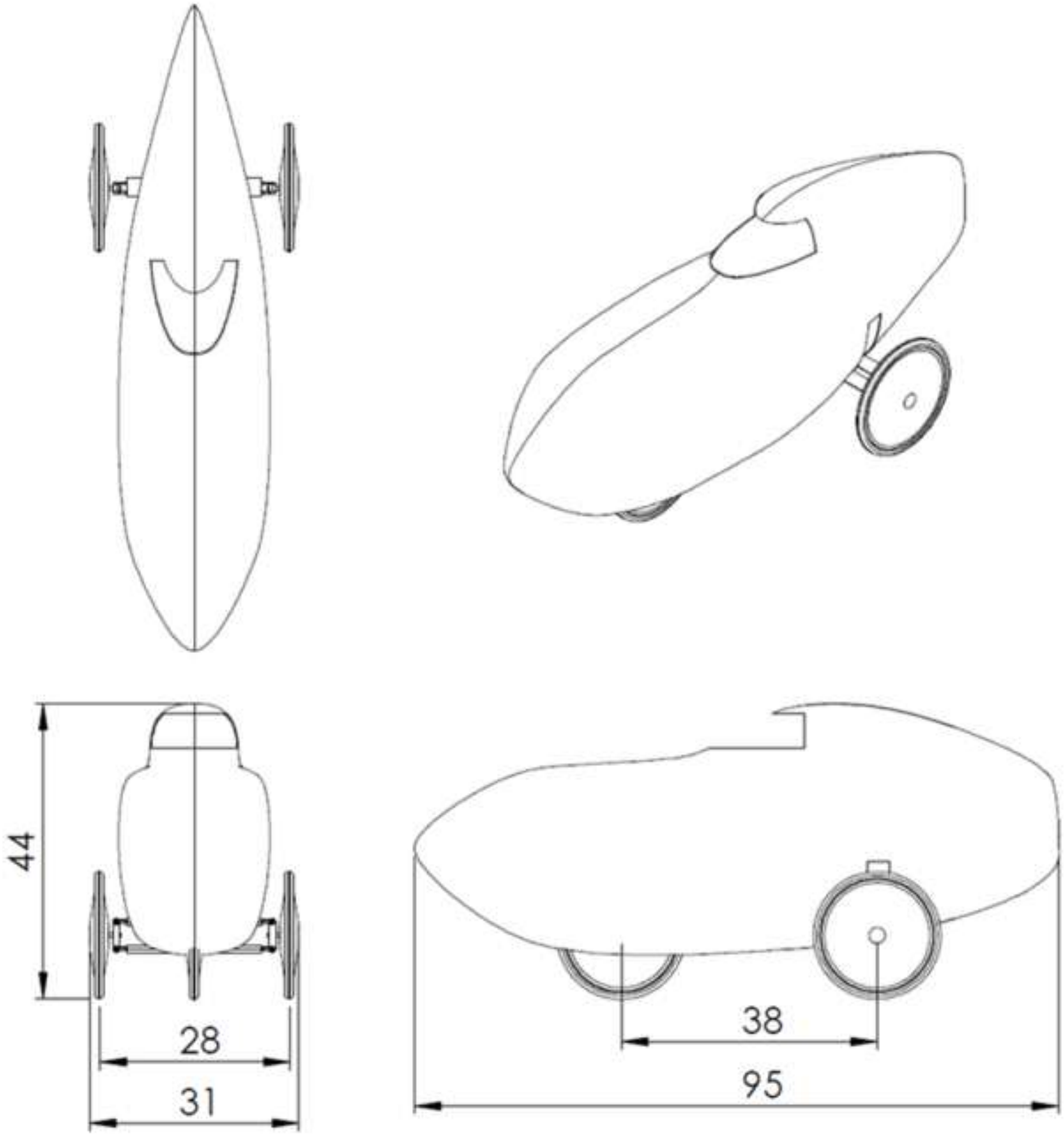

All dimensions are in inches.

Abstract

During the 2013-2014 competition season, the Rose-Hulman Human Powered Vehicle Team designed and constructed the Namazu—a lightweight, efficient, and agile human-powered vehicle that can safely and effectively be used for everyday transportation. The project's scope included all aspects of vehicle design and fabrication. The team conducted analysis, computational modeling, and physical testing to demonstrate that the Namazu met the safety and feature requirements of Rose-Hulman Institute of Technology, Human Powered Race America events, and the ASME Human Powered Vehicle Challenge.

Within these requirements, the team designed Namazu with the objectives of exceptional performance, practicality, and safety. The vehicle is a semi-recumbent delta-style tricycle with a carbon fiber structural fairing and a steel subframe. The fairing weighs 35 lbf (156 N) and was the product of an improved six-piece mold, which eliminated seaming.

The choice of standard bicycle components and sub-frame made of rectangular 4130 steel tubing increased reparability and durability. The team designed Namazu to have excellent stablity at all speeds from 0 to 50 mph, an innovative electronic rear-wheel steer system, and an energy storage system for giving the rider an extra speed boost. These features combine with a backpack-sized storage space, standard lighting, a flag, and a horn to make the Namazu a highly practical vehicle.

The team held rider safety paramount in the design of the Namazu. The vehicle boasts a forward field of vision of 200 degrees and a protective layer of Kevlar to guard against penetrating debris. Both its three-point ratcheting safety harness and maximum top load on the roll bar tested at twice ASME specifications. The team also introduced an innovative independent rear-wheel steering system to improve maneuverability. With robust and novel engineering, the Namazu advances the field of human-powered vehicles.

Table of Contents

1 Design

1.1 Objective

The Rose-Hulman Human Powered Vehicle Team (HPVT) designed, tested, and constructed Namazu during the 2013-2014 academic year guided by the team's mission statement:

> The Rose-Hulman Human Powered Vehicle Team has the goals of furthering the field of human powered vehicles, creating a common library of knowledge pertaining to their design and construction, developing innovative processes and designs, and providing a positive learning and working environment for students.

The design goals for Namazu were to maximize efficiency, speed, and practicality for safe personal transportation.

1.2 Background

As energy costs have increased, so too has the demand for sustainable forms of transportation. Commuter use of unfaired upright bicycles has increased 47% between 2000-2011 [1]. Unfaired upright bicycles are an economical and efficient mode of transportation, but they do not offer the same safety and convenience features as automobiles. Bicycles have low top speeds and offer little in terms of storage space and safety features.

Namazu—a faired, recumbent, lockable-tilting tricycle—captures the practical and safety features of automobiles while maintaining the efficiency and sustainability of unfaired upright bicycles. Its design improves upon the stability of an upright while achieving the higher possible speeds of a recumbent. A structural, aerodynamic fairing further increases the speed of the vehicle and protects the seat-belted rider better than a normal bicycle. The vehicle boasts sizeable storage space, a comfortable seating position, and a stored energy drive system. These features combine to make Namazu a more practical, efficient, and faster alternative to unfaired upright bicycles.

1.3 Prior Work

The following is a list of features and processes the team developed in previous years that were used in the creation of Namazu.

Wind conditions used in the CFD analysis of the 2010 Ragnarök were repeated for the fairing design of Namazu [2].

A 3D motion capture processing program, originally developed for the 2011 Helios, was reused to generate a model of the space required inside the vehicle for the rider. This method was used to ensure that the fairing would fit closely around the rider without interfering with the rider’s natural pedal stroke [3].

Namazu uses the ribbed tub monocoque concept of the 2012 Carɳot Cycle and 2013 Celeritas for the structural fairing. The team has verified this rib layout with the isotropic analysis in ANSYS and orthotropic analysis in Siemens NX performed in 2012. Stability of Namazu was analyzed using a MATLAB program developed for the 2012 Carŋot Cycle. The snap-fit method used on the 2012 Carŋot Cycle to ensure the hatches were even with the fairing was also used for Namazu [4]. Namazu uses a commercially-fabricated seat belt mounted to the fairing via five steel rivets through an aluminum plate. Using this mounting method, five specimens were tested to failure in 2012. Using Student's t-test, the 95% confidence interval on the ultimate strength was 810 ± 100 lbf (3600 ± 400 N) [4]. Namazu has three mounts giving 1100 lbf (4900 N) in ultimate strength, meeting the 2014 HPVC requirement of 750 lbf (3340 N).

The front hatch design of the Namazu uses the front hatch design of the 2013 Celeritas. Similar to the 2013 Celeritas, the rear hatch of Namazu is attached to the vehicle with magnets with the addition of a secondary mechanical attachment method described in Section 1.8. The hand calculations used to verify Namazu's bottom bracket integrity were developed in 2013 [5].

1.4 Organizational Timeline

The team created a Gantt chart to plan the development process for Namazu. The Gantt chart, shown in Figure 1, was updated periodically to reflect changes and delays.

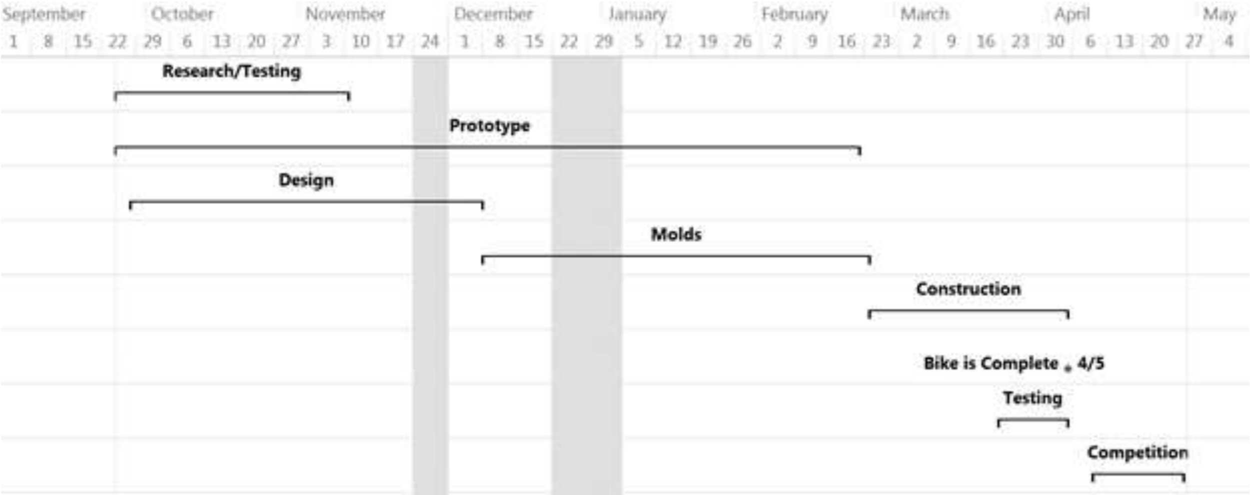

Figure 1: Gantt Chart Summary for 2014 Competition Season

1.5 Design Specifications

The team compiled design constraints for Namazu from ASME HPVC, Rose-Hulman, Indiana state law, and the Human Powered Race America (HPRA) rules and regulations. These constraints are summarized in Table 1.

Table 1: Namazu Design Constraints

Source	Constraint
ASME HPVC [6]	1. Cargo area able to hold a 15 x 13 x 8 inch (38 x 33 x 20 cm) parcel 2. Braking from 15 to 0 mph (25 to 0 kph) in less than 20 ft (6.0 m) 3. 26 ft (8.0 m) turning radius 4. Rider safety harness with ultimate tensile strength over 750 lbf (3340 N) 5. Unassisted starts and stops 6. Roll bar with elastic deformation of less than 2 in (5.1 cm) for a 600 lbf (2.67 kN) top load and less than 1.5 in (3.8cm) for a 300 lbf (1.33kN) side load 7. Stability at 3-5 mph for 100 ft (5-8 kph for 30m) 8. Rollover protection system that lessens impact and prevents abrasion in crash
Rose-Hulman	1. Molds routable out of standard 4 x 8 ft (1.02 x 2.44 m) pieces of foam on school router 2. Total cost of materials and consumables less than $10,000 3. No exposed carbon fiber near rider 4. School colors paint scheme (red, white, and black)
Indiana State Law [7]	1. For riding at night, white front lamp and red rear lamp/reflector visible from 500 ft to front and rear, respectively 2. Bell or other device audible from 100 ft (30 m)
HPRA [8]	1. Independent and redundant braking system 2. Rear-view mirrors

The team used Quality Function Deployment (QFD) to decide design goals for Namazu. Team members took a survey to rank need statements and conducted a sensitivity analysis on the scoring rubric in 2014 HPVC Rules. The needs were then prioritized and matched with metrics in a House of Quality, shown in Figure 2.

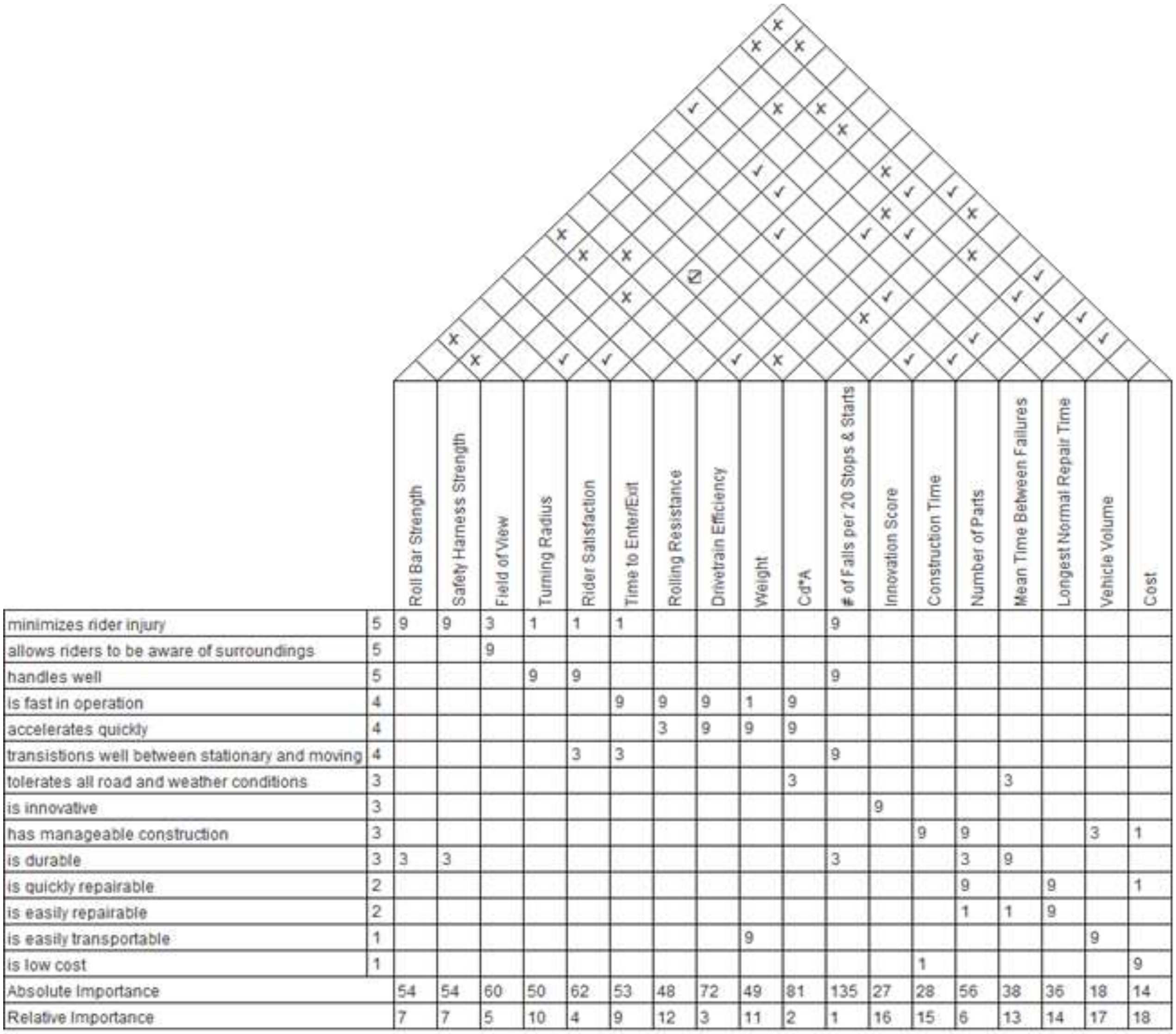

		Roll Bar Strength	Safety Harness Strength	Field of View	Turning Radius	Rider Satisfaction	Time to Enter/Exit	Rolling Resistance	Drivetrain Efficiency	Weight	Cd*A	# of Falls per 20 Stops & Starts	Innovation Score	Construction Time	Number of Parts	Mean Time Between Failures	Longest Normal Repair Time	Vehicle Volume	Cost
minimizes rider injury	5	9	9	3	1	1	1					9							
allows riders to be aware of surroundings	5			9															
handles well	5				9	9						9							
is fast in operation	4						9	9	9	1	9								
accelerates quickly	4							3	9	9	9								
transistions well between stationary and moving	4					3	3					9							
tolerates all road and weather conditions	3										3					3			
is innovative	3												9						
has manageable construction	3													9	9			3	1
is durable	3	3	3									3			3	9			
is quickly repairable	2														9		9		1
is easily repairable	2														1	1	9		
is easily transportable	1									9								9	
is low cost	1													1					9
Absolute Importance		54	54	60	50	62	53	48	72	49	81	135	27	28	56	38	36	18	14
Relative Importance		7	7	5	10	4	9	12	3	11	2	1	16	15	6	13	14	17	18

Figure 2: Namazu House of Quality

From the House of Quality, the team developed product design specifications (PDS) to guide the design of Namazu. The PDS are shown in Table 2.

.

Table 2: PDS Sorted by Priority Given by House of Quality

Metric	Marginal value	Target value
falls in 20 stops and starts	1	0
C_dA (ft^2)	1.2	0.6
part count	100	80
drivetrain efficiency (%)	90	98
rider satisfaction (1-10 scale)	7	10
field of view (deg)	270	360
time to enter/exit (s)	15	3
mean time between failures (hrs)	10	50
turning radius (constraint) (ft)	14	6
weight (lbf)	80	50
construction time (weeks)	7	5
cost (excluding labor) ($)	7,000	5,000
rear-wheel track (in)	32	26

The team chose PDS to retain positive characteristics of previous vehicles. The allowable frequency of falls during stops and starts was held especially low to make Namazu safer for the rider, more practical as a vehicle, and better able to start and stop without assistance. Maximum track (distance between the two rear wheels) was specified at 32 inches (81 cm) so that Namazu could easily fit through most doors [9].

1.6 Concept Development & Selection Methods

The team evaluated five systems to fulfill the established PDS. The first and second were tricycles with the two wheels in front (tadpole) or in back (delta). The last three were bicycles with different subsystems for stability: an open top rather than a closed fairing, two-sided landing gear, and fabric slits that allow riders to extend their legs outside of the vehicle. The team used a weighted decision matrix (shown in Figure 3) to help determine which solution to pursue.

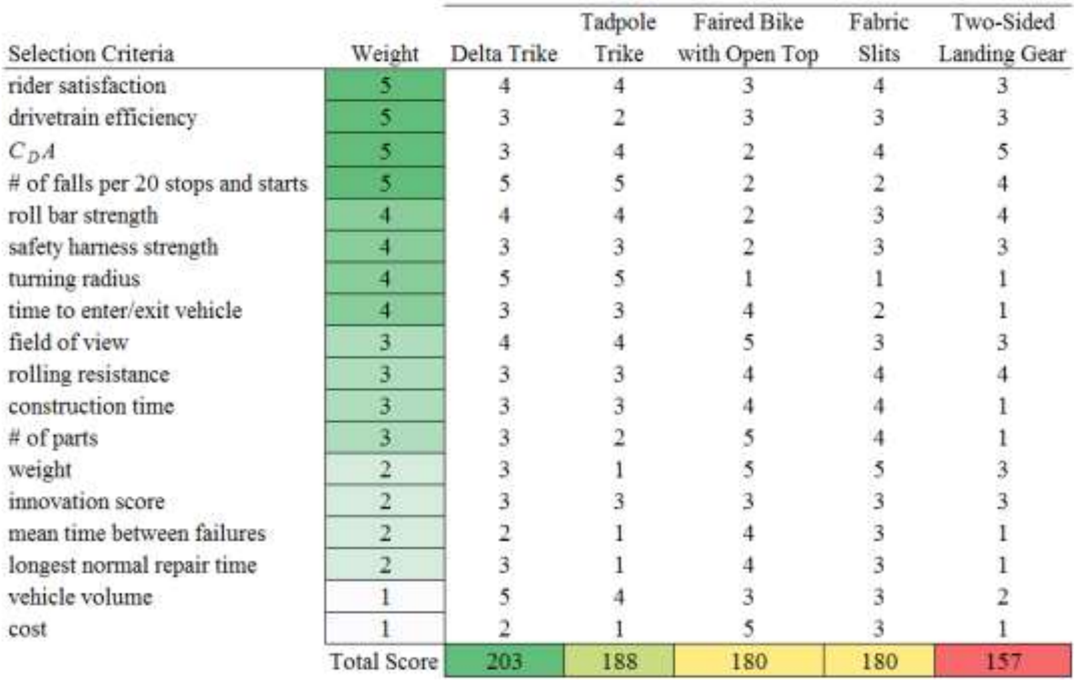

Selection Criteria	Weight	Delta Trike	Tadpole Trike	Faired Bike with Open Top	Fabric Slits	Two-Sided Landing Gear
rider satisfaction	5	4	4	3	4	3
drivetrain efficiency	5	3	2	3	3	3
$C_D A$	5	3	4	2	4	5
# of falls per 20 stops and starts	5	5	5	2	2	4
roll bar strength	4	4	4	2	3	4
safety harness strength	4	3	3	2	3	3
turning radius	4	5	5	1	1	1
time to enter/exit vehicle	4	3	3	4	2	1
field of view	3	4	4	5	3	3
rolling resistance	3	3	3	4	4	4
construction time	3	3	3	4	4	1
# of parts	3	3	2	5	4	1
weight	2	3	1	5	5	3
innovation score	2	3	3	3	3	3
mean time between failures	2	2	1	4	3	1
longest normal repair time	2	3	1	4	3	1
vehicle volume	1	5	4	3	3	2
cost	1	2	1	5	3	1
	Total Score	203	188	180	180	157

Figure 3: Decision Matrix for Basic Namazu Design Platforms

The decision matrix indicated the delta trike as the superior option for the design of Namazu. The team also desired that the vehicle be able to take turns quickly. The team achieved this with a tilting mechanism for the tricycle. Based on research of other HPV manufacturers like John Marciglio and Greg Kolodziejzyk and previous team experience with the 2010 Ragnarök, the team chose a parallelogram mechanism to enable Namazu to lean [10] [11].

1.7 Innovation

1.7.1 Rear-wheel steer

The tilting delta trike design combines the favorable high speed handling characteristics of an upright with the low speed stability of a tricycle. To counter the limited maneuverability of the 2010 Ragnarök, Namazu employs rear-wheel steering in addition to its customary front-wheel steering.

The rear-wheel system uses a potentiometer to sense the angle of the front wheel, allowing a microcontroller to send an appropriate control signal to the large servo motor mounted on a rear steering mechanism. The servo moves the rear-steering linkages back and forth to steer the wheels. The rear-wheel steer system decreases the minimum turning radius of Namazu from 136 to 45 inches (340 to 110 cm) and improves the handling, as detailed in Section 3.3.2.

1.7.2 Stored Energy Drive

Other HPVC teams have developed a stored energy drive system, but very few have effectively utilized such a system during a race. The prototype for the 2012 Carηot Cycle had regenerative braking, but it required unrealistically long stretches of braking to store usable amounts of energy. The team hypothesized that an alternate system would allow the rider to store energy at the start of a sprint race and then discharge the energy in a time trap to increase their final speed.

This is analogous to what a Namazu rider could do outside of the HPVC: store energy either from pedaling or from the grid into the vehicle and discharge it on a commute.

The storage system uses a transmission between the pedals and the mid drive to direct power. When the rider wants to store energy (for example, at a stop light), they shift the transmission to charge mode which routes their pedaling power from the front wheel to a motor. This motor generates electrical power and stores it in a bank of ultra-capacitors, increasing their voltage. Unlike batteries, these ultra-capacitors can discharge to zero volts at the start of a race so that the system can be used exclusively on human power.

When the rider has finished generating power, they shift the transmission to drive mode, in which the system behaves as it would on any other bicycle. At any point in drive mode, the rider can discharge the stored energy. The energy that is stored in the ultra-capacitors transmits through a boost converter to keep the output voltage at a constant 24 V as the voltage of the ultra-capacitors decreases. The energy then passes through a speed controller to allow the rider to adjust the power with a thumb throttle. Finally, the energy is discharged through the charging motor to assist in propelling the vehicle.

Though the system can discharge when the rider is not pedaling, it is optimized for when a rider is pedaling at 90 RPM. For the sprint event at 2014 HPVC West, analysis detailed in Section 2.5.3 shows that the stored energy drive system increases Namazu’s top speed from 36 to 44 mph (58 to 71 kph). The system will be fully removed from Namazu for the 2014 HPVC endurance races.

1.8 Fairing and Frame Design

The Namazu frame is a ribbed tub monocoque similar to those of the 2012 Carηot Cycle and the 2013 Celeritas. The ribbing throughout the vehicle is constructed from a Nomex honeycomb core wrapped in one sheet of unidirectional carbon fiber. The ribs are laid up in a continuous line to increase their strength; this is possible because Namazu is manufactured using a six-piece mold and therefore is seamless [5]. The ribbed tub monocoque frame design allows the team to use an aerodynamic shell made of composite materials as the bulk of support structure, reducing the overall weight. The remaining support comes from the steel subframe to which the front wheel and pedals are mounted. The team favored steel over carbon fiber for the subframe because of steel’s high manufacturability and ease of attachment.

As described in Section 1.3, Namazu has a removable front hatch similar to that of the 2013 Celeritas that allows for easy rider ingress and egress and the removal of the steel subframe. Based on the 2013 Celeritas, the front hatch allows Namazu to meet its PDS value of 15 seconds for time to enter the vehicle. Namazu will likely exceed this specification due to the greater stability afforded by the trike design, compared to the landing gear of the 2013 Celeritas.

The one-sided rear hatch of the 2013 Celeritas limited access to the rear of the vehicle and was prone to falling off. This year, that issue has been resolved by using a modified version of the rear hatch on the 2012 Carηot Cycle. Namazu has a double-sided rear hatch to allow greater access to the vehicle’s rear storage space, electrical equipment, and tilting mechanism. A twist latch and snap-fit secures the rear hatch to Namazu.

1.9 Roll Bar

An integrated composite roll bar protects the rider of Namazu. The design is similar to that of the 2013 Celeritas, but the outer layer of Namazu's roll bar is a carbon fiber-hybrid weave instead of simple carbon fiber. This protects the structural layers of the roll bar from abrasion without increasing weight or cost. The layup order of the composites is shown in Figure 4.

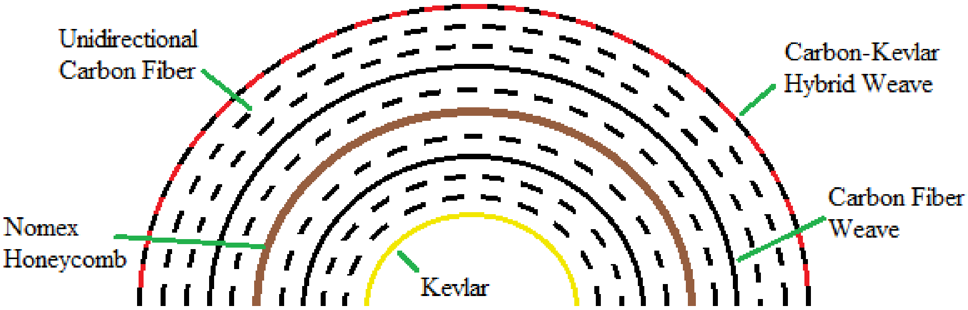

Figure 4: Roll Bar Components

1.10 Trike Mechanism

Namazu is a tilting delta trike to increase its practicality. As detailed in Section 1.6, the team researched different trike mechanisms developed by hobbyists and consulted several team alumni on their experience with the 2010 Ragnarök.

The team constructed a prototype, shown below in Figure 5, with rear wheels supported by two parallel struts in a four-bar mechanism. The ends of the parallel struts are attached to the wheels via aluminum steering knuckles. The mechanism attaches to the subframe via two rods that extend through bearings located in the center of each strut. The assembly pivots about the two rods, keeping the wheels parallel to the fairing as it leans. When the rider wants to remain upright, they actuate a hydraulic brake with a brake lever on the tiller. The brake clamps on a brake disc mounted to the strut, holding Namazu upright. The brake lever is fitted with a locking mechanism to allow the rider to leave the vehicle locked for extended periods. The lock mechanism gives Namazu both low-speed stability and high-speed performance.

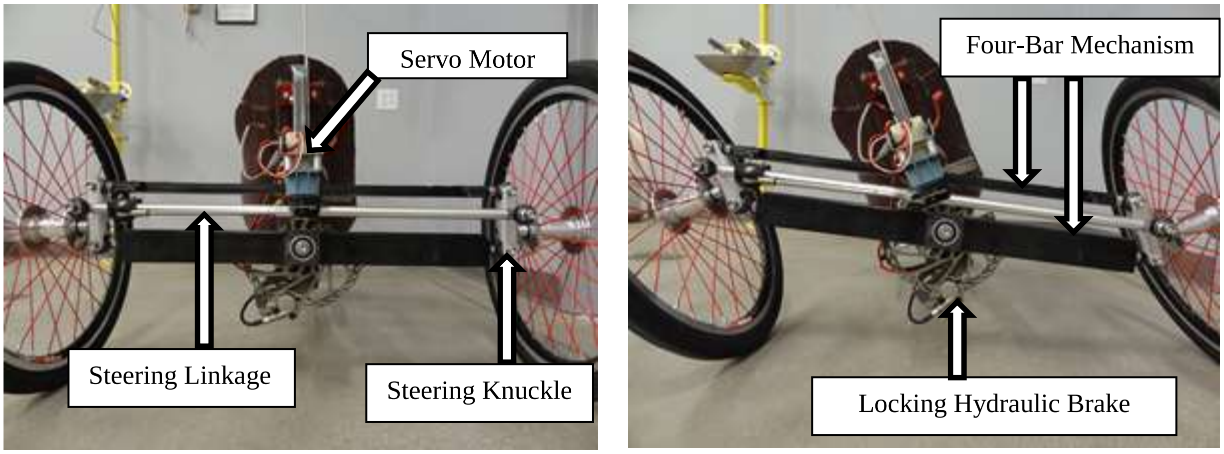

Figure 5: Prototype Trike Mechanism (locked upright on left, leaning on right)

1.11 Drivetrain

Namazu required a drivetrain with sufficient clearance for the energy capture motor and gearbox. The 2013 Celeritas used a specially designed low Q-factor front wheel drivetrain with narrowly-spaced pedals, which would leave very little room for the stored energy drive system. Because of this, the team returned to a normally-spaced drivetrain, which has the added benefit of reducing drivetrain complexity. From research on similar systems, the team concluded that it met its PDS value of 95% on drivetrain efficiency [12].

1.12 Six-Piece Mold

The team used a six-piece mold in the production of Namazu, similar to the 2013 Celeritas. Using this method, the vehicle fairing was created in one week with three layups, compared to the two-week, four layup and seaming process used for the 2012 Carηot Cycle and its predecessors. The three layups of the six-piece mold method are as follows: one to create the front and back hatch, one to create the top two-thirds of the vehicle, and a final layup to build the bottom third of the vehicle. See Figure 6 and the 2013 Celeritas Design Report for further description on the development and functionality of the basic six-piece mold [5].

For Namazu, the team improved the vacuum bag design due to troubles with the six-piece mold process during construction of the 2013 Celeritas. Last year, the team built a bag that fit inside the mold and could be taped to the top side of the box that aligns the mold pieces. Unfortunately, sealing the seams between the mold pieces proved difficult. To avoid this problem this year, the team used a bag large enough to enclose the entire box, which had the added benefit of keeping the carbon fiber to be laid up in the second stage from contacting any epoxy in the first stage.

The 2013 Celeritas molds were covered with homemade gel-coat made out of talcum powder and epoxy. In small-scale testing, this mixture created a hard surface, but it peeled off the foam during manufacturing and vacuum bagging. To improve the durability of the mold surface, the team instead applied two layers of 10 oz. (280 g) fiberglass to the surface of the mold and sanded it smooth.

Figure 6: Fairing Layup Steps: Hatches (left), Top Two-Thirds (middle), and Bottom Third (right)

1.13 Practicality

The team designed Namazu to be both an HPVC racing vehicle and a practical means of personal transportation. In its construction, standard bicycle components were used where possible for ease of replacement. The composite fairing resists corrosion and can be patched if punctured.

With its tilting trike and locking mechanisms, Namazu is stable in all riding conditions. The internal volume of Namazu is larger than the 2013 Celeritas, allowing the rider to move more freely while in the vehicle, suiting the PDS of Namazu. These features combine to produce a highly practical vehicle.

1.13.1 Storage

The cavity directly behind the rider is used for storage, as with prior vehicles such as the 2012 Carηot Cycle and 2013 Celeritas. However, the trike design of Namazu greatly expands the storage area due to the lack of a rear wheel in the fairing, as with previous vehicles. The storage space is easily accessible through the rear hatch and measures greater than 15 x 13 x 8 inches (38 x 33 x 20 cm), meeting the team's PDS. It can accommodate a non-rigid airplane carry-on.

1.13.2 Weather Conditions

Namazu provides comfort for the rider in a variety of weather conditions. The team determined temperatures from 40°F (4°C) to 95°F (35°C) to be the reasonable conditions for riding. This range extends past 80°F (27°C) because of a NACA air duct which ventilates the rider while riding. Because of this vast range, Namazu is rideable throughout most of the continental United States. The 2014 HPVC locations of Orlando, FL and San Jose, CA are almost always within this range of temperatures, ignoring average lows which usually occur overnight, when riding is unlikely to take place. The fairing provides much more protection from precipitation than a conventional trike, but the slick road conditions associated with precipitation are not ideal for riding. According to weather data for Terre Haute, Indiana, the team's headquarters, Namazu would be rideable approximately 330 days per year [13].

1.13.3 Communication

Namazu has a headlight, turn signals, brake lights, and horn to allow the rider to interact with the world outside the fairing. The headlights are visible at night from over 500 ft (150m) and the horn is audible from over 100 ft (30 m). These meet the constraints imposed by Indiana state law (shown in Table 1). Additionally, Namazu is equipped with a two-way radio during competition to allow the rider to communicate with team members.

2 Analysis

2.1 Rollover Protection System

Objective	Method	Results
Verify the strength of the rollover protection system keeping the rider safe	Deflection estimate obtained via hand calculations	The roll bar meets ASME specification with a top load deflection of 0.18 in (4.6 mm) and a side load deflection of 0.36 in (9.1 mm)
	ANSYS was used for FEA to determine deflection in two load cases	The roll bar meets ASME specification with a top load deflection of 0.45 in (11.5 mm) and a side load deflection of 0.64 in (16.4 mm)

The team analyzed the roll bar through hand calculations using Castigliano's method and Finite Element Analysis (FEA) to ensure that the roll bar met specifications given in Section III.C.1 of the ASME competition rules [6]. The team simplified the model by assuming left-right symmetry, omitting the Nomex ribs, treating the steel cross-member as perfectly joined to the composite with no mounting hardware, and treating the composite as an anisotropic material. The composite's material properties were calculated as the area weighted average of the various components. For example, the team calculated the elastic modulus as 15.5 msi (107 GPa).

Castigliano's method with redundant reactions was used to approximate the deflection under the given loading conditions. The roll bar was discretized as a quarter circle as the top, a rod in compression and bending for the side, and a rod in compression and bending for the cross-member. The load was assumed to be vertical for the top loading condition, and the load was assumed to be horizontal for the side loading condition. The loads were located as specified in Section III.C.1 of the ASME competition rules [6]. The model and results of each are displayed in Figure 7 and Table 3, respectively.

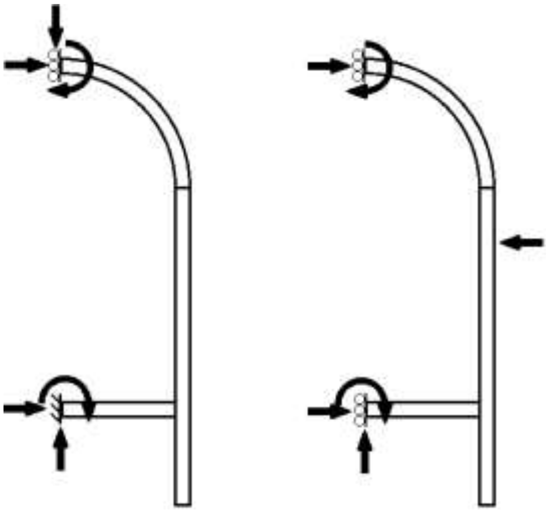

Figure 7: Roll bar Hand Calculation Models, Top (left) and Side (right)

Analysis of the top and side load was also performed in ANSYS to provide further assurance that the roll bar design would protect the rider. Static forces were applied as specified in Section III.C.1 of the HPVC rules [6]. For both load cases, the left end of the steel cross-member and the left end at the top of the model were held fixed in the horizontal direction to reflect the assumption of symmetry. For the top load analysis, the left end of the steel cross-member was held fixed in the vertical direction because this point would be held fixed during the test. The ANSYS results are shown in Figure 8, and the maximum deflections are summarized in Table 3.

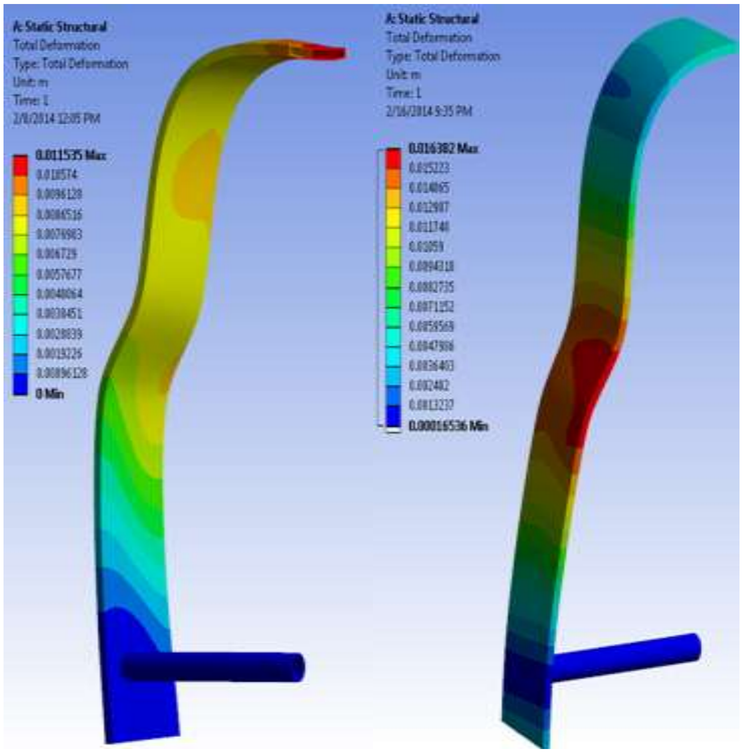

Figure 8: Results of the FEA for the top load condition (left) and side load condition (right)

Table 3: Summary of Rollover Protection System

	Deflections via ANSYS, inch (mm)	Deflections via Hand Calculations, inch (mm)
Top Load	0.45 (11.5)	0.18 (4.6)
Side Load	0.64 (16.4)	0.36 (9.1)

The discrepancy between the ANSYS model and the hand calculations is due to the simplified geometry used in the hand calculations. In both cases, the deflection is far below the 1.5 in (3.8cm) required by the HPVC Rules [6].

2.2 Structural Analysis

Objective	Method	Results
Determine the amount of material necessary to support the loads on the steel sub-frame	Hand calculations to determine steel dimensions capable of handling the bending load	Rectangular 1 x 1 ½ inch steel tubing with a wall thickness of 0.065 inch is sufficiently strong for the subframe
	FEA to estimate stresses and deflections	Only two attachment points are necessary for the subframe.

The Namazu frame is a ribbed tub monocoque with a steel subframe. As described in Section 1.3, the team used previous structural analysis for the strength of the Nomex ribs and the bottom bracket from the 2012 and 2013 competition years, respectively [4] [5]. The 2013 Celeritas subframe was suspected to have a factor of safety less than 6 so the team looked to create a stronger design and decrease the stress for this year's subframe. A design with a third mounting point above the bottom bracket shown in Figure 9 was chosen to increase the overall strength of the subframe. The forces, F_{BB} and F_W, and the moment, M_{BB}, come from the 2013 Celeritas design report and are 175 lb (770 N), 250 lb (1112 N), and 19 lb_f-ft (26 N-m), respectively.

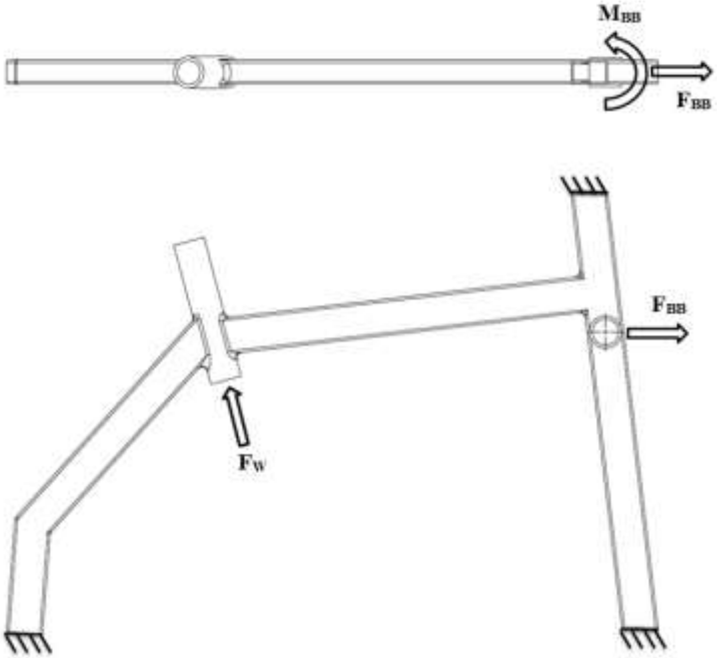

Figure 9: Forces on the subframe and fixed mounting points

Basic analysis modeled the subframe as a fixed beam with the force of the wheel, F_W, pushing up on the beam. It was assumed that all the mounts are rigidly fixed and that the force on the bottom bracket, F_{BB}, and the moment about the bottom bracket, $M_{BB,}$ had a relatively small impact on the stress in the subframe. The maximum stress was found using the bending equation below.

$$\sigma_{max} = \frac{Mc}{I} \tag{1}$$

where σ_{max} is the maximum bending stress, c is the maximum distance from the neutral axis, and I is the second moment of area of a rectangular cross section. The maximum moment, M, in the fixed beam was found to be the force F_W multiplied by the distance from the head tube to the front supports or 200 ft-lbf. From this calculation the team found that a 1 x 1 ½ in. rectangular tubing of 4130 steel with a wall thickness of 0.065 in. would have a factor of safety of 10.

The team designed a frame out of the 4130 steel tubing to match the geometry shown in Figure 9 and modeled the geometry in ANSYS with the loads from Figure 9. The ANSYS results confirmed the hand calculations and showed that the frame had a factor of safety of 10. The team wanted to lighten the frame but wanted to keep the factor of safety above 6. Through further simulations, it was found that removing the third mount above the head tube reduced more weight than changing the size of the rectangular tubing and also reduced the overall complexity of the design. The final subframe design shown below had only two mounts, a maximum deflection at the top of the head tube of 0.007 in., a maximum stress intensity of 11 ksi on the inside of elbow on the left, and an overall factor safety of 6.8 just above the team's desired factor of safety.

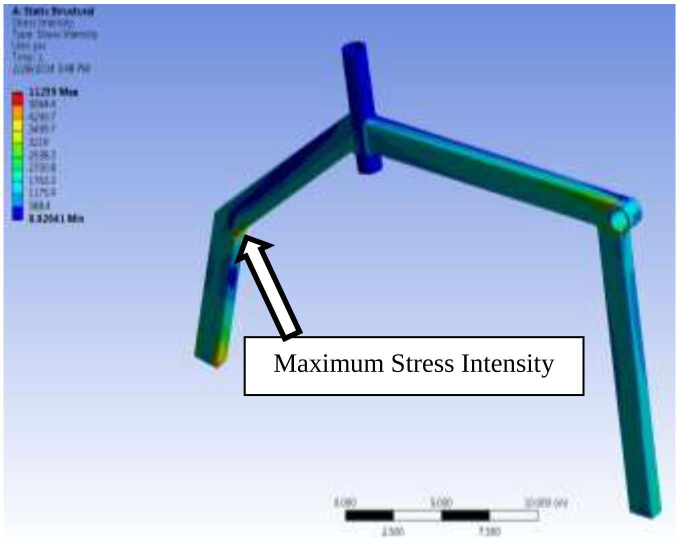

Figure 10: Frame FEA on Subframe

2.3 Aerodynamic Analysis

Objective	Method	Results
Determine the fairing shape to make Namazu easiest to pedal	SolidWorks Flow Simulation and hand calculations to determine drag forces	At 45.5 mph, Namazu fairing will see a 1.55 lbf (6.89 N) drag force. In a 13.6 mph cross wind, Namazu fairing will see a 20.5 lbf (91.1 N) lateral force.

As part of the decision process for finding the optimal vehicle platform in Section 1.6, hand calculations were done to find the drag area for five different vehicle designs. The equations for finding the drag area of various holes and exposed wheels were found in Douglas Carroll's *The Winning Solar Car* [14]. Drag areas for various tubing shapes were found in Munson's *Fundamentals of Fluid Mechanics* [15].

Table 4: CdA Values of Various Vehicle Components

	C_dA [ft^2]	Faired Bike	Tadpole Trike	Semi-faired Bike	Delta Trike	Upright Bike
2013 Celeritas body	0.27	X	X		X	
Faired Wheel	0.2		X		X	
Faired Wheel	0.2		X		X	
NACA Duct	0.018	X	X	X	X	
Rear Wheel Hole	0.011	X	X	X		
Rear Wheel Exposed	0.0004	X	X	X		
Wheel Strut	0.166		X		X	
Butterfly Hole	0.142	X		X	X	
Front Wheel Exposed	0.052	X		X	X	
Upright Bike [16]	6.05					X
Tub Body	0.7			X		
Total Drag Area [ft^2]		0.49	0.86	0.93	1.05	6.05

A delta trike has about double the drag area of a two-wheeled recumbent but one-sixth that of an upright bicycle. The team determined from the hand calculations that both the streamline body and wheel coverings were essential to an aerodynamic vehicle.

The team modeled the fairing and iteratively refined it in SolidWorks Flow Simulation. Past experience indicated that it was valid to ignore ground and wheel movement, simplifying the simulation. SolidWorks visualization tools helped identify areas of improvement. The final results of this iteration are shown in Table 5.

Table 5: Drag Force of Namazu Compared to Previous Vehicles

Fairing Shape	Force at 45.5 mph (lbf)	Lateral force with 13.6 mph cross wind (lbf)	Bike width at shoulders (in)
Namazu	1.55	20.5	19.7
Celeritas (2013)	1.47	26.6	18.4
Carηot Cycle (2012)	1.66	24.6	19.8

The final Namazu fairing performs within 6% of the 2013 Celeritas while increasing interior space for the rider. From the hand calculations shown in Table 4 and SolidWorks simulation results in Table 5, the estimate $C_D A$ for Namazu is 1.05 ft^2, below the PDS marginal value of 1.20 ft^2 (0.11 m^2).

2.4 Cost Analysis

Objective	Method	Results
Determine the cost of producing Namazu and the cost of a three-year production run	Created a financial account of parts, materials, overhead, labor, tooling, and capital investment	Namazu cost $17,650 to produce as-presented including labor, and would cost $9,700 per vehicle for a production run.

The costs associated with producing the Namazu as-presented and the cost for a 3 year, 10 vehicle per month production run are summarized in the tables below.

Table 6: Cost Breakdown of Major Vehicle Components

Section	Materials	Skilled Labor Hours	Materials + Labor Costs
Drivetrain	$1,504.00	10	$1,704.00
Fairing	$1,897.00	70	$3,297.00
Foam and Fiberglass Molds	$1,017.00	360	$8,217.00
Subframe	$117.00	10	$317.00
Rear Wheel Steer	$521.00	35	$1,221.00
Stored Energy Drive	$1,355.00	40	$2,155.00
Electronics	$57.00	15	$357.00
Safety/Comfort Features	$125.00	12	$365.00
Material Costs	$6,593.00	Materials + Labor	$17,633.00

Table 7: Total Cost for Production Runs of Namazu

Material Costs for 360 Vehicles	$1,710,000.00
Labor Costs for 360 Vehicles	$1,040,000.00
Overhead Costs for 360 Vehicles	$639,000.00
Tooling Costs for 360 Vehicles	$39,700.00
Capital Investment for 360 Vehicles	$54,000.00
Total Costs	$3,480,000.00
Cost Per Vehicle	$9,670.00

The cost of materials for Namazu includes both costs incurred by the team and estimates for donated goods. The material costs total $6,593, which fell beneath the PDS marginal value of $7,000. Labor estimates were taken from detailed meeting records and an assumed average hourly wage of $20 to obtain labor costs for the vehicle as-presented.

For a scale-up production of 360 vehicles over three years, new costs arise, but existing costs decrease. New costs include capital, tooling, and overhead. Capital costs include heavy machinery, workspace/warehouse leasing, and all purchased tools that were expected to last the duration of the production. Tooling costs include the price of tools needing replacement either after every build or periodically during production. Overhead costs include office space rental, insurance, and additional staff. Labor and material costs for scale-up were estimated to decrease 25% and 15% respectively due to process optimization and bulk-volume purchasing. Molds were considered durable as constructed for the competition vehicle and were treated as a one-time cost for materials and labor. Itemized production costs are given in Appendix A.

Cost for the vehicle as-presented is $17,650. The estimated cost per vehicle for a production run is $9,700. The largest contributing factor to the price reduction is the re-use of the mold, which represents 47% of the total cost of the prototype as-presented. This production cost is significantly higher than the only marketed fully-faired vehicle, the Lightning F-40, which retails for $6,100 [17]. The team considers this cost acceptable due to the increased safety of a full carbon fiber fairing as well as the greatly added utility of the included stored energy drive system.

2.5 Other Analysis

2.5.1 Gearing

Objective	Method	Results
Determine gear ratios for competition	Vehicle velocity related to pedal speed. Set the mid-drive to achieve the desired speed range.	A mid-drive gain ratio of 14:22 was found to yield the optimal speed range of 8-50 mph (11-85 kph).

The team selected gear ranges according to a comfortable cadence range of 60-120 RPM and the speeds observed in the 2013 HPVC races. The maximum and minimum sustained speeds, respectively, were 42 mph (68 kph) during the drag event and 5 mph (8 kph) in the endurance event. By a proper range of gears, Namazu achieves these speeds at the appropriate cadences.

The team used an 18.5 in (47 cm) diameter wheel, a 60 tooth chainring, and an 11–36 tooth cassette as the basis for the gearing design. From these parameters, a mid-drive gain ratio of 15:20 gave the desired output speeds. At cadences ranging from 60-120 RPM, the rider can maintain speeds between 8 and 50 mph (13 to 80 kph). A rider can maintain a speed less than 8 mph (13 kph) at a cadence below 60 RPM.

2.5.2 Stability

Objective	Method	Results
Determine trike dimensions for maximum stability during locked upright turning	MATLAB to model forces on trike while turning to maximize velocity through corners while locked upright	Within constraints of bike construction and aerodynamics, a wider rear track with rider sitting closer to the rear axle is best.

Lessening the number of falls during starts and stops was the highest priority PDS. Namazu’s tilting delta trike design easily handles most of the tight, slow corners which frequently caused riders of the 2013 Celeritas to fall. However, a trike can be tipped over when maneuvering too quickly when locked, so the team analyzed trike stability to determine trike dimensions that optimized the handling characteristics of Namazu. These dimensions are shown in Figure 11 and summarized in Table 8.

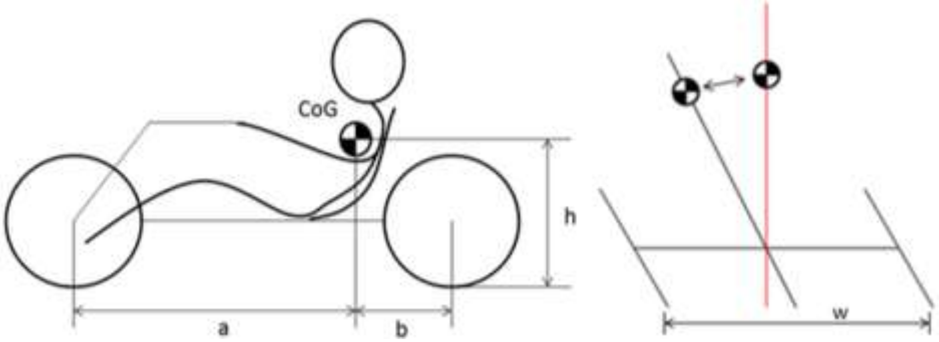

Figure 11: Dimensions Used for Dynamic Analysis

Table 8: Definitions of Trike Dimensions

Dimension	Description
a	Distance from rider center of gravity (CoG) to front wheel
b	Distance from rider CoG to rear wheel
h	CoG height of vehicle and rider
w	Rear track width

These dimensions were subject to a number of constraints. Team motion capture data identified an a of 18 inches (46 cm) for maximum power output. To maintain rider visibility through the windshield, h was fixed at 18 inches (46 cm). Fairing dimensions limited b to 20-24 inches (51-61 cm). Finally, the PDS for track width limited W to less than 32 inches (81 cm) so to allow Namazu to fit through standard interior doorways [9]. Figure 12 shows the relationship between b, w, and the maximum speed for the 26 ft (8 m) radius turn mandated by the 2014 HPVC when locked upright.

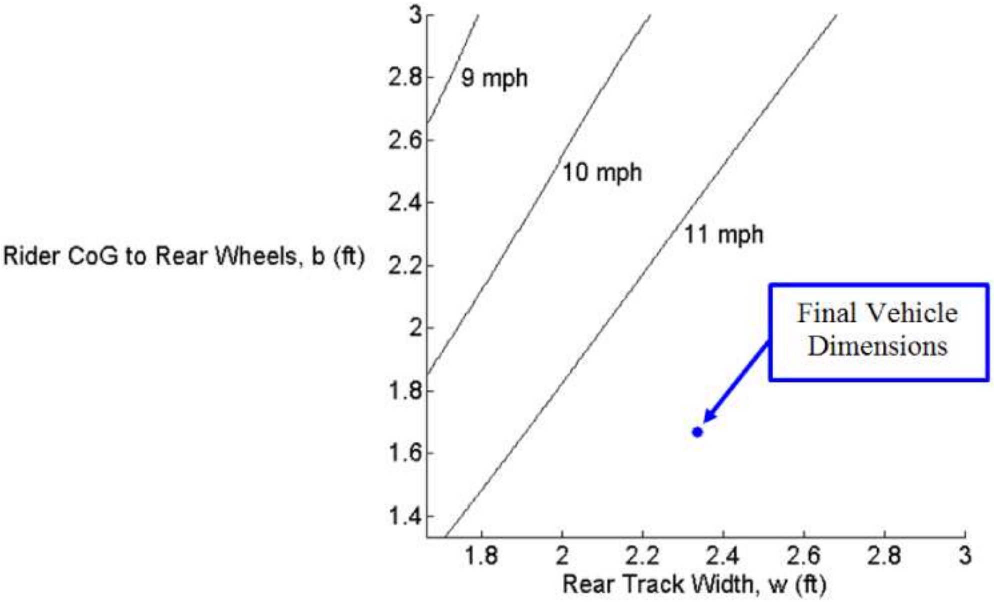

Figure 12: Dimension Optimization of b *and* w *to Maximize Cornering Speed*

Stability analysis indicated that a distance of 21 inches (53 cm) from the rider center of gravity to the rear wheels and a rear track width of 28 in (71 cm) would allow Namazu to travel around an 26 ft (8 m) radius turn at 12 mph (19 kph), meeting the PDS for turning radius.

2.5.3 Power-Speed Modeling

Objective	Method	Results
Determine the performance increase with stored energy drive system.	Create a force balance MATLAB model with drag coefficients from testing. Validate with previous year's sprint race results.	The stored energy drive system will increase Namazu's speed by 9 mph on the 2014 HPVC West sprint course

The team created a force balance MATLAB Simulink model to predict Namazu's performance in the sprint race with the stored energy drive system. Based on conservation of linear momentum, the model implemented the equation

$$ma = \frac{P}{v} - C_D A v^2 - \mu_{rolling} mg \tag{2}$$

where m is the estimated vehicle and rider mass, a is the acceleration, P is the power applied through the drivetrain, v is the velocity, $C_D A$ is the drag area, $\mu_{rolling}$ is the rolling resistance coefficient. The drag coefficients $\mu_{rolling}$ and $C_D A$ were determined from coast down testing with the 2013 Celeritas, detailed in Section 3.2.4.1. The team estimated the mass of Namazu as 80 lbm (36 kg) and its $C_D A$ at 1.05 ft^2 (0.066 m^2) based on comparisons to Celeritas and analysis detailed in Section 2.3.

To determine the baseline rider performance in the model, the team examined the performance of Celeritas in the 2013 HPVC West sprint event. The run-up distance was around 1600 ft (480 m), and the team's fastest male rider went through the time trap at 38 mph (61 kph). The power-speed modeling suggests that this required an average of 500 W (0.67 hp).

Based on the efficiencies of the stored energy drive system and constraints of the 2014 HPVC West sprint event, the team expects the motor to deliver 600 W (0.80 hp) of additional mechanical power for a duration of 21 seconds. The results of this power boost when performed right before the time trap are shown in Figure 13.

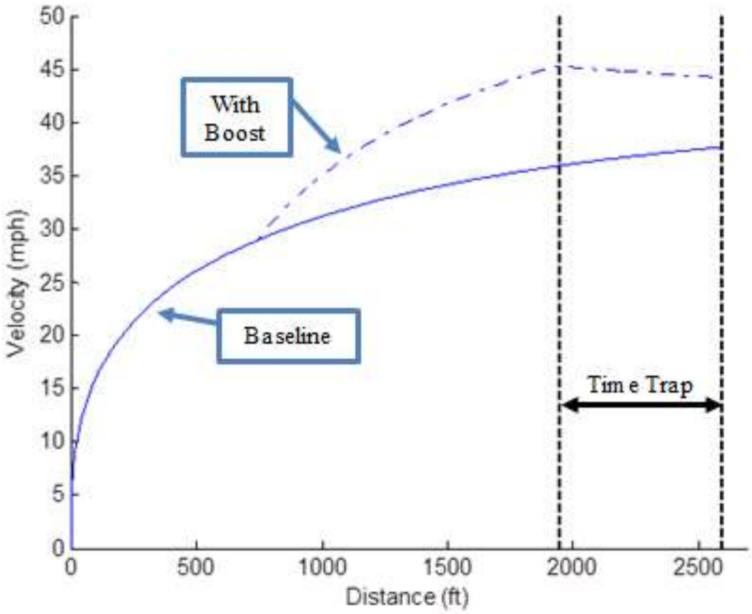

Figure 13: Modeled Velocity for the 2014 HPVC West Sprint Event

The power-speed modeling shows that with the stored energy drive system, Namazu will complete the time trap at 44 mph (71 kph) rather than the 36 mph (58 kph) it would achieve at baseline power—a benefit which outweighs its weight and complexity.

3 Testing

3.1 Rollover Protection System Testing

The team conducted roll bar testing to confirm the Rollover Protection System (RPS) Analysis and to ensure that the RPS meets specifications of the 2014 HPVC rules [6]. The team applied loads as specified in HPVC Rules to a duplicate RPS using an ATS 1610 tensile tester and measuring the resultant deflection. The team constructed the duplicate RPS with the same materials, geometry, and process as the RPS in Namazu. The RPS testing results fall in between hand calculations and ANSYS simulation results, as seen in Table 9.

Table 9: Deformation in the roll bar

	Elastic Deformation, inch (mm)		
	Hand Calculations	ANSYS Workbench	Tensile Testing
Top Load—600 lbf (2670 N) at 12° from vertical towards aft	0.18 (4.6)	0.45 (11.5)	0.33 (8.4)
Side Load—299 lbf (1330 N) horizontally at location of shoulder	0.36 (9.1)	0.64 (16.4)	0.47 (11.9)

No permanent deformation occurred when loaded to HPVC specifications, evidenced by post-test height measurements and the lack of visible or audible indicators during the test. The team also tested the RPS to failure in the top load condition, reaching a maximum load of 1120 lbf (4.98 kN). The Namazu RPS meets and exceeds the constraints imposed by the 2014 HPVC.

3.2 Developmental Testing

3.2.1 Micro-rib Testing

On past vehicles, flat regions of the fairing had low lateral stiffness, resulting in susceptibility to damage and high road noise. The team tested micro-rib designs to add rigidity with minimal additional weight. Using existing processes, small Nomex or foam ribs could be added to the skin but would substantially increase manufacturing time. As a faster alternative, the team also considered mass-produced materials such as plastic fencing which could be placed in the vehicle during a layup.

The team made four different micro-rib sample groups and tested them using a four-point bending test. Each group had four 6 x 9 inch (15 x 23 cm) samples with a different internal reinforcement material sandwiched between two layers of 11 oz. carbon fiber.

The first group used a small plastic mesh with 1 inch (2.5 cm) square holes for reinforcement. The second experimental group was reinforced using 0.25 inch (0.6 cm) thick Nomex ribs cut into triangles. The third group was a control group which had no additional internal reinforcement material. The final group used a large plastic mesh with 1.5 inch (3.8 cm) square holes for reinforcement. A sample from each group is shown below in Figure 14.

Figure 14: Micro-rib Testing Samples (From left to right: 1 inch square mesh, triangular ¼ inch Nomex rib, flat/control, and 1.5 inch mesh)

The samples were weighed and a 4-point bend test was conducted to find their bending stiffness. The results are summarized in Table 10.

Table 10: Summary of Micro-rib Testing

	Average Weight, oz.	Average Sample Strength, lbf	Strength to Weight Ratio
1 inch holes	1.093±0	17.0±3.3	249
Nomex	0.917±0.074	33.6±3.8	586
Flat (control)	0.575±0.028	2.4±0	67
1.5 inch holes	0.988±0.048	13.6±1.7	220

The team found that mesh ribs were significantly easier to manufacture than the Nomex ribs, because the Nomex ribs needed to be chamfered while the mesh could just be laid down in correctly-sized sheets. Unfortunately, the plastic mesh was heavier and weaker than Nomex ribs; the strength-to-weight ratio for the Nomex ribs was double that of the mesh structure and was much better than the previous year's unreinforced carbon. The team found that the strength increase of the Nomex ribs over the mesh structure justified the extra fabrication time.

These test results indicate that triangular Nomex ribs are the most effective way to increase the stiffness of the skin. As a result, Nomex micro-ribs are placed as needed to stiffen the skin of Namazu. An informal survey of riders suggests that this will increase rider satisfaction, a product design specification.

3.2.2 Skid Testing

Extensive sliding during crashes poses a significant danger to the rider and causes wear to the vehicle. The 2013 Celeritas and 2012 Carɳot Cycle used automotive trim to lessen skidding, but the team determined that it would not use trim because it was less durable than desired and did not have consistent material properties. The team tested neoprene rubber strips of various hardness ratings to determine if any would be a suitable replacement.

The rubber strips were attached to a 1 ft (0.3 m) long carbon fiber skid rig and loaded to 120 lb (533 N) to simulate half the weight of the occupied vehicle on the proper size of contact patch. The team measured the force required to drag the rig at a constant 5 mph (8 kph). A material passed the braking test if it exerted more than the 120 lbf (530 N) required to safely stop the vehicle from top speed in 150 feet (45 m). This distance was chosen because it mirrors the clear distance available to skid after the time trap of the Hellyer Park Velodrome, the 2014 HPVC West sprint race site, which the team identified as the most dangerous potential crash site this season. The durability of the rubber strips was then tested by dragging the sled 1500 ft (760 m) loaded with the full vehicle weight of 240 lb (1.1 kN) to simulate 10 high-speed crashes. The material passed the test if more than one-quarter of the material remained. The results of the testing are shown in Table 11.

Table 11: Skid Testing Results

	50A Hardness Neoprene	60A Hardness Neoprene	70A Hardness Neoprene	Bare Carbon Fiber
Braking Force Test	Passed	Passed	Passed	Failed
Durability Test	Failed	Failed	Failed	Failed

All tested options except for the bare carbon fiber control passed the braking force test and were viable for skid-prevention. Although all the tested options failed the durability test, the 70A Hardness Neoprene strips exhibited the least wear, and so were considered the best choice. They have been implemented on Namazu in place of auto trim to increase rider safety and decrease the PDS of mean time between failures.

3.2.3 Crash Testing a Crumple Zone

The rigidity of Namazu enables its fairing to protect the rider from striking obstacles in a collision, but this same rigidity worsens whiplash. The team conducted preliminary crash testing to determine if different possible configurations of a nose cone could serve as a crumple zone and significantly lessen the force on the rider during a collision. Doing so would help meet the team's foremost need of minimizing rider injury. The tested configurations are shown in Figure 15.

Figure 15: Nose Cone Configurations: Insulation Foam, Cushion Foam, Single and Double Layer Fiberglass

After establishing a control, the team attached each configuration to the 2009 Mark IV, crashed the unoccupied vehicle into a wall. The team measured the pre- and post-collision speeds by comparing the frame-by-frame position of the vehicle relative to a striped board.

The ability of each configuration to function as a crumple zone was correlated to how quickly the vehicle rebounded after collision at a set initial velocity. Assuming a constant impact duration across nose cone designs, a lower change in velocity meant that the design caused the rider to experience less acceleration and vice-versa.

No nose cone design performed significantly better than the control. Significant work remains to design the crumple zone on an HPV and prove its effectiveness.

3.2.4 Aerodynamic Testing

For the past five years of competition, the team has estimated drag area values using computational fluid dynamics (CFD), but with no experimental data for model validation. This year, the team experimentally determined vehicle $C_D A$ using two methods. The team had three objectives with these tests: verify the computer simulations, examine different vehicle body designs, and determine the aerodynamic impact of varying the rear wheel width of Namazu.

3.2.4.1 Coast Down Testing

The first method of determining $C_D A$ was a coast down test on the 2013 Celeritas. For twelve trials, the team accelerated the vehicle to over 30 mph (48 kph) and allowed it to coast to below 8 mph (12.9 kph). A bicycle computer recorded velocity and time data during each coast down.

The team ran a non-linear regression on the combined data to determine the $C_D A$ and the uncertainty in the test. Both the data from the twelve trials and the non-linear regression are shown in Figure 16.

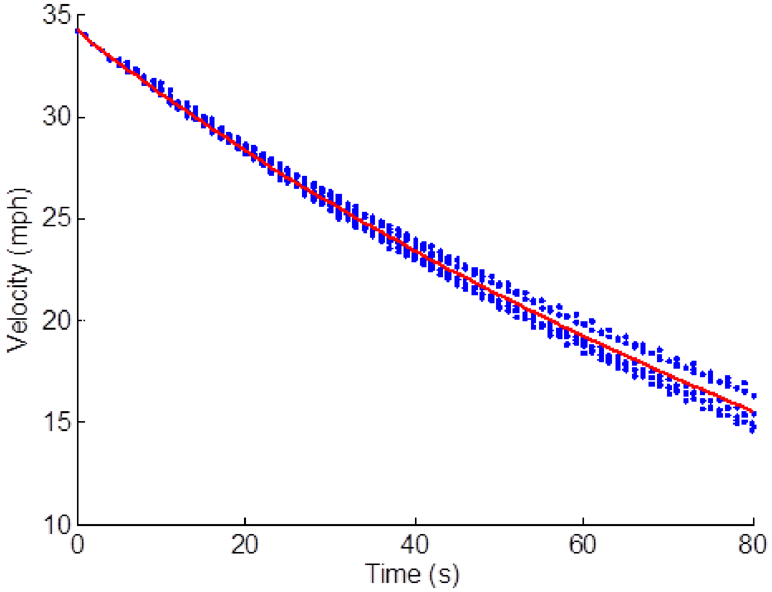

Figure 16: Coast Down Test Results (Data Points in Blue, Non-Linear Regression in Red)

The coast down test yielded a 95% confidence interval on $C_D A$ of 0.7±0.1 ft^2 (0.06±0.01 m^2) for the 2013 Celeritas. Systematic uncertainty came mostly from uncertainty in atmospheric temperature and contributed 91% of total uncertainty. Random uncertainty contributed the remaining 9%. The likeliest source of random uncertainty is the wind speed, which varied from 0.0-0.7 mph (0.0-1.1 kph) across all trials. For further details, see “Coast-Down Testing of a Rose-Hulman Human Powered Vehicle” in Appendix B.

The empirical value for $C_D A$ of the 2013 Celeritas was used in the power-speed modeling (described in Section 2.5.3) to give a more accurate representation of Namazu’s performance. Also, the team refined the modeling techniques in the Solidworks Flow Simulations (detailed in Section 2.3) so that the model of Celeritas produced an empirically accurate value for $C_D A$.

3.2.4.2 Wind Tunnel Testing

The team used a 3D printer to manufacture one-eighth scale models of the 2012 Carηot Cycle and 2013 Celeritas and tested the models in a wind tunnel. The team measured airspeed in the tunnel with a manometer, atmospheric temperature with a barometer, and the drag force with a load cell, and could thereby solve for $C_D A$. For further details, see “Measuring the Drag Area of a Human Powered Vehicle” in Appendix C.

The wind tunnel testing yield $C_D A$ of 0.65 ± 0.03 ft^2 (0.060 ± 0.003 m^2) for the Carηot Cycle and 0.57 ± 0.03 ft^2 (0.053 ± 0.003 m^2) for Celeritas. Both coast down and wind tunnel testing revealed that the $C_D A$ values which the team has determined from CFD are unrealistically low, emphasizing the necessity of empirical verification. Based on the testing, the likely $C_D A$ of the

2013 Celeritas is 0.60 ft^2 (0.056 m^2). This is close to the C_DA value of 0.49 ft^2 given by hand calculations for the 2013 Celeritas in Table 4, so the team can conclude that the hand-calculated C_DA of 1.05 for Namazu is similarly accurate. Namazu thereby falls within the PDS range for C_DA of 1.20-0.55 ft^2 (0.11-0.05 m^2).

Wind tunnel testing had a lower random uncertainty than coast down testing because of the controlled test environment and a lower systematic uncertainty because of the higher precision equipment used. Its drawbacks were that the testing did not account for the drag effects of surface roughness, wheel holes, or the thin posts which held the models in the center of the tunnel. These inaccuracies made it difficult to project the true C_DA of Namazu prior to its construction. However, because these effects could be held constant across trials, wind tunnel testing was ideal for distinguishing the effects of rear wheel track width on the C_DA of Namazu.

From research, the team knew that interference between the boundary layers of the rear wheels and the fairing would cause a low pressure region behind Namazu and potentially increase drag force [11]. To study this effect, the team created a properly scaled model of the rear wheels and struts and mounted it on the model of the 2012 Carηot. The team performed further wind tunnel testing and varied the rear wheel track width to examine its effect on C_DA.

The team determined that increasing rear wheel track width up to 32 in (81 cm) decreases the C_DA. This was most likely due to the decreased interference between wheel and fairing boundary layers. Beyond that width, the results would need to be extrapolated. However, the PDS placed limits on track width so that Namazu could fit through a doorway and navigate a slalom.

3.3 Performance Testing

3.3.1 HPVC Obstacle Testing

The team tested the Namazu prototype against different obstacles to determine Namazu's readiness for the 2014 HPVC. Two team members rode the Namazu prototype through a quick turn and washboard road set up per HPVC rules. They remained stable and at-speed through all of them for six trials. From this, the team can conclude that Namazu will have no difficulties with these obstacles at the 2014 HPVC.

The team set up the slalom course specified by the ASME Rules. The first slalom test had riders of the Namazu prototype closely follow another vehicle which would stop at an unplanned time. The riders performed twenty trials of these emergency starts and stops without falling, meeting the highest priority PDS.

The team also timed the riders on final Namazu prototype racing through the slalom. On the same layout, the team also rode a recumbent bicycle and the first Namazu prototype, which was constructed earlier in the competition season. Compared to the final iteration, the first prototype had a higher center of gravity, shorter wheelbase, and shorter track—all features that Stability Analysis showed to increase tipping potential while locked. This test had the additional objectives of verifying Stability Analysis results and the team's initial decision to design a tilting delta tricycle rather than its customary bicycles. The slalom results are displayed in Figure 17.

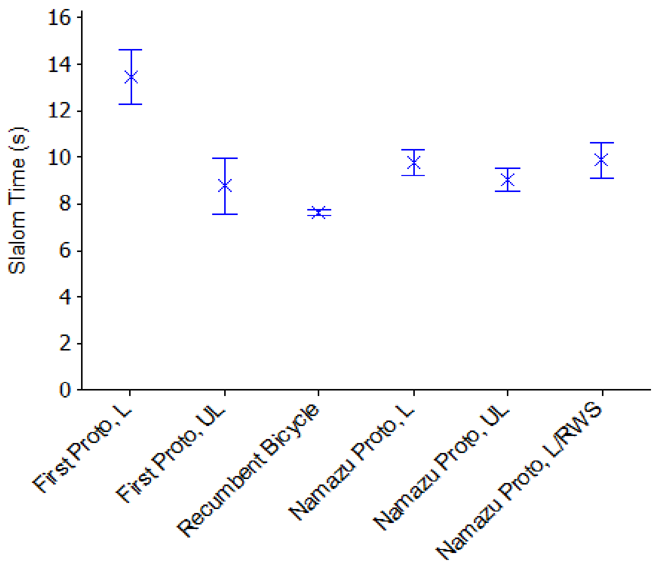

Figure 17: Slalom Testing Mean Times and 95% Confidence Intervals
(L = Locked, UL = unlocked, RWS = Rear Wheel Steer Active)

The team performed a series of One-Way ANOVA tests to determine if any vehicle configurations were significantly faster through the slalom. The p-values for notable statistical tests are shown in Table 12.

Table 12: Results of ANOVA Tests on Slalom Times for Pairs of Vehicle Configurations

Configuration 1	Configuration 2	p-value	Conclusions
First Proto, Locked	First Proto, Unlocked	<0.001	The tilting mechanism is valuable in decreasing slalom time.
Namazu Proto, Locked	Namazu Proto, Unlocked	0.023	
First Proto, Locked	Namazu Proto, Locked	<0.001	The final dimensions that Stability Analysis yielded increase stability
Namazu Proto, Unlocked	Recumbent Bicycle	<0.001	The wide track of Namazu makes it slower through the slalom than a recumbent bicycle. However, this difference is not more than 2.5 seconds.
Namazu Proto, Locked	Namazu Proto, Locked with rear wheel steer	0.84	The team cannot conclude the addition of rear wheel steer makes Namazu faster in the slalom.

Slalom testing showed that implementing a lockable leaning system and altering Namazu's final dimensions based on stability analysis significantly decreased slalom time. The same could not be concluded about the rear wheel steer system. When above 7 mph (11 kph), vehicle dimensions matter far more to handling than the direction the rear wheels point.

Slalom testing also showed that designing Namazu as a tricycle instead of bicycle hampered its minimum time through a slalom. However, the 2.5 s maximum difference per run is far better than dozens of time-consuming, slow-speed crashes that plagued the 2013 Celeritas.

3.3.2 Turning Radius Testing

The team tested the turning radius of the Namazu prototypes while locked upright across different scenarios to verify the predictions of stability analysis and ensure it met the turning radius PDS of 15 ft (4.5 m). In the first subtest, the team set up a circle of cones and had riders go as fast as they could staying inside of the cones and keeping all wheels on the ground. The circle radii and their maximum speeds were recorded and are shown in Table 13.

Table 13: Tight Cornering Performance

	Top Speed (mph) within 26 ft (8 m) Radius	Top Speed (mph) within 16 ft (5 m) Radius
First Prototype	8	6
Namazu Prototype, no rear wheel steering	12	7
Namazu Prototype, rear wheel steering	13	8

The addition of rear wheel steering to Namazu did not significantly improve its high speed cornering ability. This confirms the slalom testing results in HPVC Obstacle Testing. However, there was a 33% increase in cornering ability from the first prototype to the final Namazu prototype. The 12 mph (19 kph) that the Namazu prototype reached matched the Stability Analysis predictions. Furthermore, riders felt more confident in cornering because of the decreased potential to tip, boosting the PDS of rider satisfaction.

The second subtest had riders make the smallest possible turn at whatever speed they could remain stable. The results for Namazu and comparable vehicles are shown in Table 14.

Table 14: Turning Radius Test at Minimum Speed

Vehicle	Turning Radius (in)
2013 Celeritas [5]	156
Namazu prototype, no rear wheel steering	136
Recumbent bicycle with no fairing	120
First prototype	76
Namazu prototype, with rear wheel steering	45
Upright bicycle	35

All Namazu prototypes have a sharper turning radius than the 2013 Celeritas, as one would expect from a tricycle which is stable at all speeds. The long wheelbase of the Namazu prototype, however, limits improvement. The first prototype had a shorter wheelbase which made it more prone to tipping when traveling above walking speed, but also gave it a low turning radius at minimal speed. The tightest turning radius belonged to the Namazu prototype with rear wheel steering. The system decisively overcomes any downsides to a longer wheelbase. It reduces turning radius by two-thirds compared to the prototype without rear wheel steering, giving Namazu a turning radius comparable to an upright bicycle and 27 inches (69 cm) under the PDS target value of 6 ft (8 m).

4 Safety

4.1 Design for Safety

In the design of Namazu, the safety of the rider and team members was of the utmost importance. All components, vehicle systems, and manufacturing methods were evaluated for their safety prior to implementation.

4.1.1 Roll Bar

A composite roll bar is included in Namazu to ensure the safety of the rider in a rollover or side impact collision. The roll bar prevents contact between the rider and the road surface and lessens the impact in a crash. With its protective layer of carbon fiber-hybrid weave, the design of the roll bar improves upon that of previous years and exceeds the competition requirements.

4.1.2 Windshield

The vehicle's windshield is made of high-strength polycarbonate and is riveted to a Nomex rib around the edges. Because of this, the windshield is secure, durable, and protects the rider while riding and during a crash. The windshield is designed in a semi-circular shape identical to that of the 2013 Celeritas. This gives a total of 200 degrees of visibility through the windshield alone and 300 degrees when combined with the rear-view mirrors, exceeding the 180 degrees requirement detailed in Section III.J of the HPVC Rules [6].

4.1.3 Seat Belt

The seat belt on Namazu is a three-point harness similar to that used on the 2013 Celeritas. It is secured in the same fashion as the 2013 Celeritas, with the top point riveted to a steel plate that is attached to the roll bar. The lower two points are attached to plates embedded in the fairing. This ensures that the rider is safe in a crash. From the testing described in Section 1.3, the three mounts of the seat belt in Namazu are sufficient and ensure that the rider is safe in a crash.

4.1.4 Safety of Manufacturing

The team educated all members on the safe use of power tools and implemented standard safety procedures. Members were not permitted to work alone or in high-traffic locations when using power tools, and were required to use proper personal protective equipment (PPE) while working. Examples of PPE include the use of respirators when sanding composites, welding equipment when MIG welding, and safety glasses at all times. Finally, the team used non-toxic materials like epoxy resin and painted in a ventilated paint booth.

4.2 Hazard Analysis

The safety of the rider is held paramount when considering any of the components that make up the vehicle. All riders are required to wear a helmet when in the vehicle. As shown in Section 3.1, the fairing can withstand side impact and rollover situations. The rider is protected by a roll bar, a roll hoop surrounding their feet, and a stiffened mid-rib at the legs. Additional flanges extend forward from the roll bar protect riders' arms during a crash with the top fairing removed.

Kevlar 5120 fabric lines the cockpit where the rider sits. In the event that the carbon fiber splinters, the Kevlar traps the splinters and prevents rider injury [2]. Sharp edges that developed during the manufacturing process were either removed or covered by rounded edging.

Uncontrolled skidding after a fall can be more dangerous than the fall itself. To reduce skidding, neoprene rubber was placed at the points of the fairing which contact the ground in a crash. The rubber also protects the fairing's structural integrity against abrasion.

To help the rider communicate their intentions and make their presence known to other vehicles and pedestrians, standard equipment such as headlights, taillights, brake lights, turn signals, side reflectors, and a loud electronic horn have been installed. The vehicle's low height makes it less visible on the road. To improve the visibility of the vehicle, there is safety flag mount on the vehicle's rear.

5 Aesthetics

Namazu is painted mostly the colors of Rose-Hulman: black, red, and white. As well as hosting the logos of the Team's sponsor, the fairing boasts an image of Namazu the Earthshaker, a catfish from Japanese mythology. Rubber strips mounted to the side of Namazu preserve the outward appearance of Namazu.

From the inside and outside, Namazu appears clean and functional. All cable and wires are integrated into the frame or fairing. The front hatch, where the rider enters and exits the vehicle, has a snap-fit design. The cover is tight enough that it will not unintentionally bounce off while the vehicle is in motion. The rear hatch provides access to the storage compartment, with a capacity of approximately a non-rigid airplane carry-on.

6 Conclusion

6.1 Comparison

Table 15: Evaluation of Namazu against PDS

Metric	Marginal/Target value	Actual value	In-text Justification
falls in 20 stops and starts	1/0	0	Slalom Testing
C_dA (ft^2)	1.20/0.60	1.05	Aerodynamic Analysis/Testing
part count	100/80	TBD	
drivetrain efficiency (%)	90/98	93	Drivetrain
rider satisfaction (1-10 scale)	7/10	8	
field of view (deg)	270/360	300	Windshield
time to enter/exit (s)	15/3	10	Fairing and Frame Design
mean time between failures (hrs)	10/50	TBD	
turning radius (constraint) (ft)	15/6	3.7 ft	Turning Radius Testing
weight (lbf)	80/50	TBD	
construction time (weeks)	7/5	TBD	
cost (excluding labor) ($)	7,000/5, 000	6,593	Cost Analysis
rear-wheel track (in)	32/26	28	Stability Analysis

6.2 Evaluation

Throughout the year, the team regularly evaluated the design of Namazu against the PDS and revised any designs which did not meet the marginal values. Namazu was not completed by the submission of this report, but it has met or exceeded all applicable PDS. Furthermore, Namazu either currently meets or will meet all constraints imposed by HPVC, Rose-Hulman, HPRA and Indiana state law.

6.3 Recommendations

The team recommends performing stability analysis concurrently with fairing design to optimize both aerodynamics and stability. If not previously constrained, stability analysis would have recommended a longer distance from the rider center of gravity to the front wheel and shorter distance from the rider center of gravity to the rear wheel.

The team also recommends performing wind tunnel testing on a scaled model of its vehicles prior to the onset of manufacturing to verify CFD models before it is too late to change. The team was unable to perform this testing this year because of time constraints. It would also be very beneficial for Namazu to be put through a coast down test after the 2014 HPVC and for the uncertainty in this test to be decreased.

Nose cone testing did not produce any design modifications to Namazu, but the team recommends that work continues on the concept.

6.4 Conclusion

The Rose-Hulman Human Powered Vehicle Team set out to create an efficient, fast, and practical human powered vehicle that could be safely and effectively used for everyday transportation. Meeting these goals required a lightweight vehicle, so Namaza uses advanced composite materials for an exceptional strength-to-weight ratio in its fully structural fairing. Namazu is highly efficient compared to an upright bicycle, requiring seven times less power to overcome air drag at the same speeds. It can travel over 45 mph (74 kph) due to its streamlined body, yet it has excellent low-speed maneuverability with its lockable tilting mechanism. Namazu has a stored energy drive system that increases its usability in a variety of situations. Most importantly, it protects the rider with its rollover protection system, safety harness, and Kevlar lining. Namazu’s combination of efficiency, safety, and practicality makes it a viable form of everyday transportation.

7 References

[1] NuAira, "Resarch," 2011. [Online]. Available: http://nuaira.com/research.

[2] Rose-Hulman Human Powered Vehicle Team, "2010 HPVT Design Report- West - Ragnarök," Terre Haute, 2010.

[3] Rose-Hulman Human Powered Vehicle Team, "2011 HPVT Design Report - West - Helios," Terre Haute, 2011.

[4] Rose-Hulman Human Powered Vehicle Team, "2012 HPVT Design Report - West - Carηot Cycle," Terre Haute, 2012.

[5] Rose-Hulman Human Powered Vehicle Team, "2013 HPVT Design Report - West - Celeritas," Terre Haute, 2013.

[6] American Society of Mechanical Engineers, "Rules for the 2014 Human Powered Vehicle Challenge," 2014.

[7] Indiana State Legislature, "Chapter 11: Bicycles and Motorized Bicycles," 2013. [Online]. Available: http://www.in.gov/legislative/ic/2010/title9/ar21/ch11.html.

[8] Human Powered Race America, "Classes and Rules," 2014. [Online]. Available: http://www.recumbents.com/hpra/rulesand.htm.

[9] C. Deziel, "San Francisco Gate: Standard Inside Door Sizes," 2014. [Online]. Available: http://homeguides.sfgate.com/standard-inside-door-sizes-84805.html.

[10] G. Kolodziejzyk, "The Rocket Lean-Steer Velomobile," 2006. [Online]. Available: http://www.adventuresofgreg.com/RocketMain.html.

[11] J. Morciglio, Interviewee, [Interview]. 2014.

[12] Cycling Power Lab, "Drivetrain Efficiency & Marginal Gains," 2014. [Online]. Available: http://www.cyclingpowerlab.com/drivetrainefficiency.aspx.

[13] The Weather Channel, "Monthly Averages for Terre Haute, IN," 2014. [Online]. Available: http://www.weather.com/weather/wxclimatology/monthly/graph/47809.

[14] D. R. Carroll, "The Winning Solar Car: A Design Guide for Solar Race Car Teams," *SAE International,* 2003.

[15] O. H. R. Munson, Fundamentals of Fluid Mechanics, New Jersey: John Wiley & Sons, Inc., 2013.

[16] Cycling Power Lab, "Cycling Aerodynamics & CdA - A Primer," 2014. [Online]. Available: http://www.cyclingpowerlab.com/cyclingaerodynamics.aspx.

[17] S. Friedlander, "Lightning Bikes," [Online]. Available: http://www.lightningbikes.com/f40/friedlander-testimonial.html.

[18] Rose-Hulman Human Powered Vehicle Team, "2009 HPVT Design Report - West - Mark IV," Terre Haute, 2009.

Appendix A: Enumerated Cost Analysis

Table A1: Detailed Tooling Costs for Namazu Production Run

Item	Cost	Amount Per Vehicle (If Consumable)	Price Per Vehicle	Price for Production Run
5 CFM Air Compressor	$550.00	-	-	$1,650.00
Bicycle Mechanic Toolset	$350.00	-	-	$1,050.00
3.2 CFM Venturi Pump	$180.00	-	-	$540.00
HSS Drill Index	$115.00	-	-	$345.00
18v Cordless Drill	$105.00	-	-	$315.00
Welding Jacket (5 ct)	$88.75	-	-	$266.25
Welding Gloves (6 ct)	$84.00	-	-	$252.00
50 ft Air Hose	$66.00	-	-	$198.00
End Mill Set	$59.80	-	-	$179.40
Carbide Tool Inserts (10 Ct)	$45.00	0.5	$22.50	$8,100.00
Safety Glasses (50 ct)	$41.50	-	-	$124.50
Dremel Rotary Tool	$41.00	-	-	$123.00
6 Inch Air Powered Rotary Sander	$40.00	-	-	$120.00
Tap and Die Set	$39.99	-	-	$119.97
Carbide Lathe Tools	$37.00	-	-	$111.00
Latex Gloves (100 ct)	$35.00	0.25	$8.75	$3,150.00
Duct Tape 2 in x 25 yd (6 ct)	$30.00	0.5	$15.00	$5,400.00
Dremel 1-1/2 Inch Cutting Wheel (12 Ct)	$20.00	1	$20.00	$7,200.00
120 Grit Sanding Discs (25 Ct)	$16.00	1	$16.00	$5,760.00
Rivet Gun	$10.00	-	-	$30.00
Popsicle Sticks (500 ct)	$8.50	0.1	$0.85	$306.00
1/8" Rivets (250 ct)	$7.90	0.2	$1.58	$568.80
Silver Sharpies (6 Ct)	$7.23	1	$7.23	$2,602.80
Plastic Cups (50 ct)	$6.50	0.5	$3.25	$1,170.00
			Total Cost	$39,681.72

Table A2: Capital Investments Required for Namazu Production Run

Item	Cost
5000 SF Industrial Space (3-year lease)	$27,500
12-Inch Shop Lathe	$2,800
12-Inch 3-Axis CNC Mill	$5,000
Floorstanding Drill Press	$1,200
60 x 30 Wood Workbench (6 total)	$1,400
Desktop Computer for CNC/CAD	$800
Millermatic 350 MIG Welder	$4,000
4 ft x 2.5 ft Welding and Jigging Table	$2,400
JET 42-Inch Milling Machine	$8,900
Total Capital Investment	$54,000

Table A3: Overhead Costs for Namazu Production Run

Staff Overhead		
	Secretary	1
	Sales Staff	1
	Wage	$25.00
	Manager	1
	Salary	$80,000.00
	Staff Overhead Sub Total:	$380,000.00
Salary Overhead		
	Total Wages	$1,424,000.00
	State/Federal Tax Rate	15%
	Taxes	$213,600.00
	Salary Overhead Sub Total:	$213,600.00
Office Facilities		
	Office Rate ($/SF/yr)	$11.00
	Office Space (SF)	1000
	Office Cost	$11,000.00
	Facilities Sub Total:	$11,000.00
Utilities		
	Monthly power rate	$100.00
	Monthly water rate	$50.00
	Phone and internet rate	$100.00
	Utilities Sub Total:	$9,000.00
Insurance		
	Estimate	$25,000.00
	Insurance Sub Total:	$25,000.00
	Overhead Sub Total:	$638,600.00

Appendix B

Coast-Down Testing of a Rose-Hulman Human Powered Vehicle

Team 4
Joel Anderson
Caleb Camara
Garrett Meyer
Sarah Vencel
CM 2340

Mechanical Engineering Laboratory
Dr. Ashley Bernal

November 15, 2013

Introduction

The Rose-Hulman Human Powered Vehicle Team (HPVT) creates high-performance recumbent bicycles but has never empirically determined their coefficient of air drag, C_d. For the past five years of competition, the value has been estimated from SolidWorks Flow Simulations or comparable programs, but this technique has resulted in widely varying reported values. The discrepancies are most likely attributed to different standards in modeling and the lack of experimental verification. Our project addresses this issue by creating a method for empirically determining C_d for Rose-Hulman Human Powered Vehicles (HPVs). This procedure will enable the competition team to describe the real-world performance of their vehicles.

Our goal is to measure the drag coefficient of a Rose-Hulman HPV to within 25% uncertainty. Studies of a similar nature have achieved this uncertainty goal, giving us initial confidence that the goal is attainable [1][2][3]. A 25% uncertainty would not distinguish one year's vehicle from another, nor between minor modifications made to the same vehicle. This would require an uncertainty below 1% [4]. However, one of the world's best faired recumbent vehicles, the Diablo, has an experimentally-determined C_d of 0.110 [5]. This is 59% greater than the reported C_d value of the HPVT's 2013 Celeritas, meaning that a 25% uncertainty could verify the claim that Celeritas distinguishes itself even among world-class vehicles [6].

Theoretical Calculations for Drag Coefficient in a Coast-Down Test

To determine a value for C_d, we ran a coast-down test. A coast-down test is performed by accelerating a vehicle to a specific speed, ceasing power to the wheels, and allowing it to coast. Velocity and time data are recorded during the coast and then used to determine the C_d value for that vehicle.

As the vehicle coasts down, it has four forces acting on it. The forces of air drag, $F_{air\,drag}$, and rolling resistance, $F_{rolling\,resistance}$, oppose the motion of the vehicle in the x-direction. In the y-direction the weight of the rider and vehicle, W, is opposed by the normal force, N, from the ground on the tires. At time, t, the vehicle rolls at velocity, $V(t)$, relative to the wind speed parallel to the vehicle's motion. The vehicle has an effective mass, m_{eff}, that incorporates the rotational inertia of the wheels. We assume in our analysis that all bearing losses are captured by $F_{rolling\,resistance}$ and that the vehicle travels on level ground. The forces and resulting acceleration are shown in Figure 1.

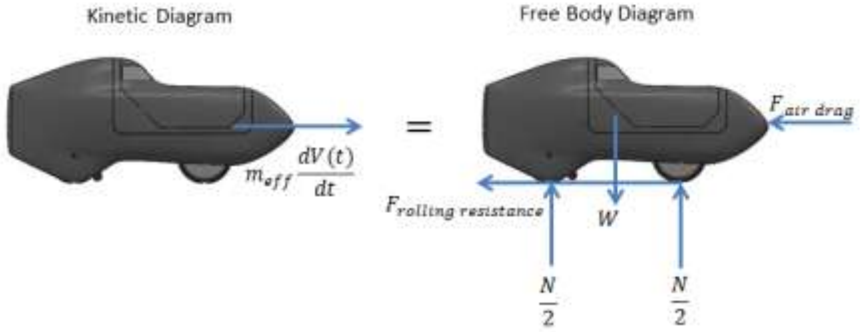

Figure 1: Free-body and kinetic diagrams for an HPV coast-down test

Applying conservation of linear momentum in the x-direction yields the overall equation of motion,

$$m_{eff}\frac{dV(t)}{dt} = -F_{\ air\ drag} - F_{\ rolling\ resistance}\ . \tag{1}$$

Using the formulas for air drag, rolling resistance, and effective mass, and considering wheels as circular disks in the calculation of their rotation inertia, (1) expands to become (2) [7]. The measurands are listed in Table 1.

$$\frac{1}{2g}\left(2W + W_{front\ wheel} + W_{rear\ wheel}\right)\frac{dV(t)}{dt} = -\frac{1}{2}C_d\frac{P}{RT}AV(t)^2 - f_rW\ , \tag{2}$$

Table 1: Nomenclature of (2)

Symbol	**Measurands**
W	Weight of rider and vehicle
$W_{front\ wheel}$	Weight of front wheel
$W_{rear\ wheel}$	Weight of rear wheel
t	Time
$V(t)$	Velocity relative to wind speed at time, t
P	Atmospheric pressure
T	Atmospheric temperature
A	Frontal area

	Constants
f_r	rolling resistance coefficient between the tires and the ground
g	Acceleration due to gravity
R	Universal gas constant
	Resultant
C_d	Drag coefficient

The motion of the vehicle is governed by (2), which contains C_d. However, C_d cannot be isolated in the equation due to the complexity of the differential equation. Therefore, a numerical approach is required. The equation of motion is solved for $V(t)$ in (3).

$$V(t) = \tan\left(\frac{-t\sqrt{C_d \frac{P}{RT} A f_r W}}{\frac{1}{\sqrt{2g}}\left(2W + W_{front\,wheel} + W_{rear\,wheel}\right)} + \arctan\left(\frac{C_d \frac{P}{RT} A V(0)}{\sqrt{2C_d \frac{P}{RT} A f_r W}} \right) \right) \sqrt{\frac{2 f_r W}{C_d \frac{P}{RT} A}} \quad (3)$$

By curve-fitting (3) to coast-down data, the least-squares approximation of C_d can be obtained, along with a 95% confidence interval that reflects its systematic uncertainty. Random uncertainty can be determined with variation in the resultant C_d across multiple trials.

Experimental System

Our testing was performed for the 2013 Celeritas Rose-Hulman HPV seen in Figure 2. Figure 3 shows the Garmin Edge 500 bike computer that was used to record velocity and time data. Velocity was measured from rotations of the wheel via a magnet and sensor. Using the GPS feature of the Garmin Edge 500 would be much less accurate because the vehicle could then only be located to within 20 ft.

Figure 2: Celeritas

Figure 3: Garmin Edge 500 Bike Computer

The frontal area of the vehicle was estimated by measuring the frontal area of the SolidWorks CAD file from which the vehicle was created [8]. Figure 4 shows a front view sketch of the 3D model.

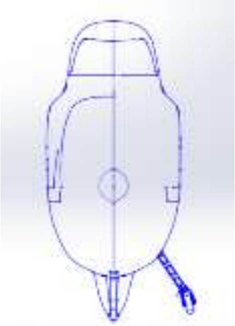

Figure 4: 3D Model Front View of Celeritas

To acquire total mass the rider lifted the vehicle and stood on a Royal 400 lb scale. We measured the mass of the wheels using an Acculab Econ 4100 g scale.

The ambient temperature and pressure were measured with a Kestrel Pocket Weather Meter 3500. This device was also used to measure wind speed parallel to the vehicle motion while a Kestrel Pocket Weather Meter 2500 measured perpendicular wind speed. The vehicle's tire pressures were checked after every four trials to ensure that they remained constant.

Though our sensor choice was first determined by convenience, it was subsequently validated by multiple shakedown tests. Each shakedown test had an uncertainty under our goal of 25%, allowing us to proceed with full confidence in our experimental design with only a few minor modifications (described in Appendix D).

Procedure

All data was collected at the Terre Haute International Airport on one section of the taxi lane shown in Figure 5. This section of the taxi lane was 0.5 miles long and has an elevation change of 2 ft. This corresponds to a slope of 0.04 degrees which allows us to assume in our analysis that the surface was flat. Test weather conditions followed the standard set in SAE J1263 [9]. Wind speed measurements were taken parallel to the taxi lane and used to adjust the velocity data collected from the Garmin. This was done because aerodynamic drag is dependent on the speed of the vehicle relative to the local air speed. All data was collected within the ambient temperature range of 41 °F – 95 °F so that all sensors could be used in their operating temperature ranges. The taxi lane was dry during the test so that rolling resistance could be assumed to be constant.

Figure 5: Terre Haute International Airport with Test Section Shown

We performed 12 trials because this met the minimum requirement of 10 trials specified in SAE J1263 [9]. During the experiment the rider accelerated the vehicle to approximately 35mph and began to coast at the start of the test section. Velocity and time data were collected during the trials. Only data collected while the vehicle was coasting between 35 mph and 10 mph was used due to noise in the velocity data at lower speeds. The speed range in this procedure is the major deviation from SAE J1263 which specified a 60 mph to 25 mph range [9]. This was acceptable because the human powered vehicle does not have rotational inertia from an engine that skews data at low speeds.

Analysis

Random uncertainty was determined by variation in the resultant across the trials. The velocity data collected was curve-fit with (3) to extract the C_d value for each trial. An example of this curve-fit is shown in Figure 6.

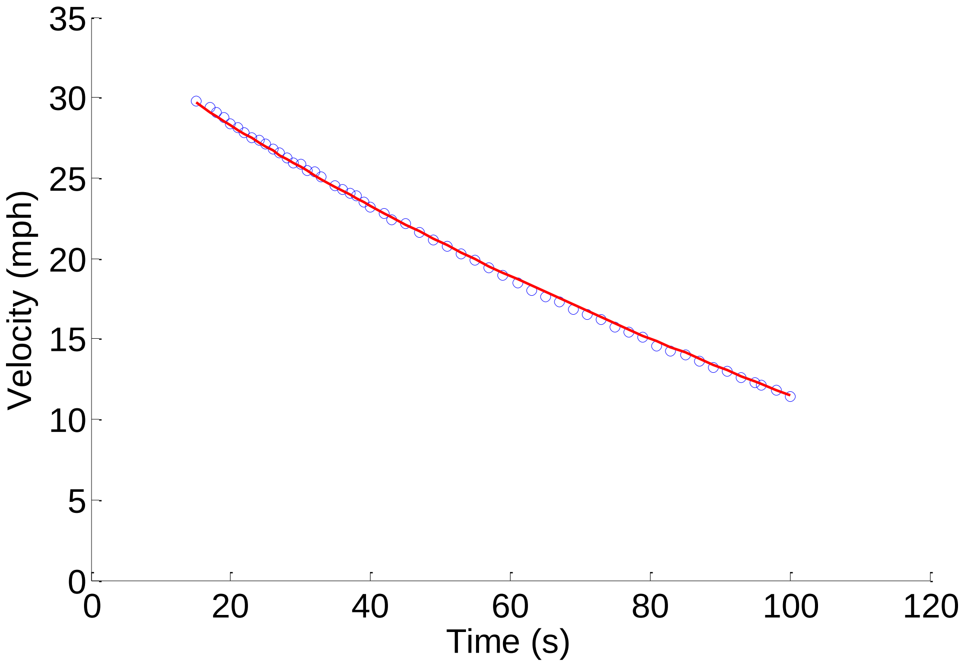

Figure 6: Coast-down data and curve-fit of a single trial

The standard deviation of the C_d values, S_{C_d} , the number of runs, n, and the Student t-statistic, t_s, combine to give

$$w_{C_d,\,rand} = \frac{t_s S_{C_d}}{\sqrt{n}} \tag{4}$$

where $w_{C_d,\,rand}$ is the random uncertainty.

Systematic uncertainty is caused by scatter in the data. When data is taken for twelve trials, there are twelve values of velocity at any given time. The scatter in the data, shown in Figure 7, requires the use of a 95% confidence interval to calculate systematic uncertainty.

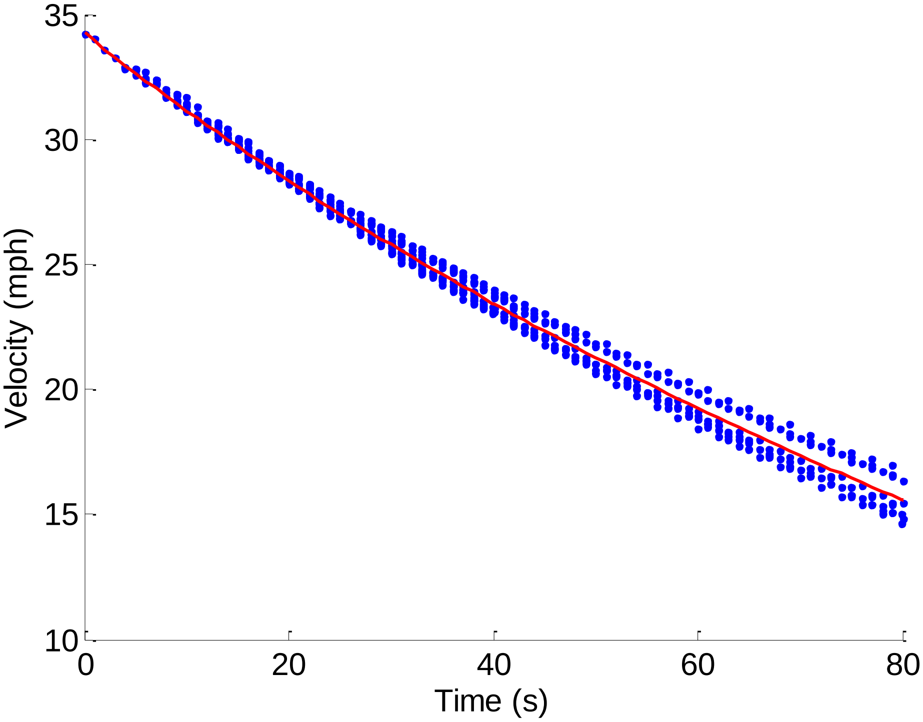

Figure 7: Single curve-fit on data from all twelve trials

The bike computer has a timer operating at a high enough frequency that uncertainty in the time measurement is assumed negligible. The uncertainty in the velocity measurements ranges from 0.2-0.6%. To account for this, each velocity measurement was tied to its uncertainty in the curve-fit. The curve-fit responded by fitting closer to more certain velocity measurements and less close to less certain ones. This increased the 95% confidence interval on C_d accordingly, allowing uncertainty in velocity to be incorporated in the total uncertainty in C_d. For more details, see Appendix A.

The curve-fit assumes precisely known values of the measurands because they determine the function (3) used to match the data. However, each measurand has an uncertainty. This means there is uncertainty not only in the velocity on which the curve-fit operates, but in the function with which it operates. To account for this fact, we first simulate five hundred values for each measurand. These values are normally distributed about the measured value and simulate what the true value of a measurand could have been given our uncertainty in the measurment. We then fit five hundred curves to the velocity data, with each curve using a simulated set of measurand values to determine (3). The output of each run was a C_d and its 95% confidence interval determined from the curve-fit. We reported the mean of these values as our resultant. We used the outputted 95% confidence interval to determine the systematic uncertainty in C_d. See Appendix C for an illustration of this process.

Results and Conclusions

Our experiment yielded a C_d of 0.18±0.03 for the 2013 HPVT Celeritas. Measurand values and their relative uncertainty are shown in Appendix B. Systematic uncertainty made up 91% of total uncertainty and random uncertainty made up the remaining 9%. This result is compared to other relevant C_d values in Figure 8.

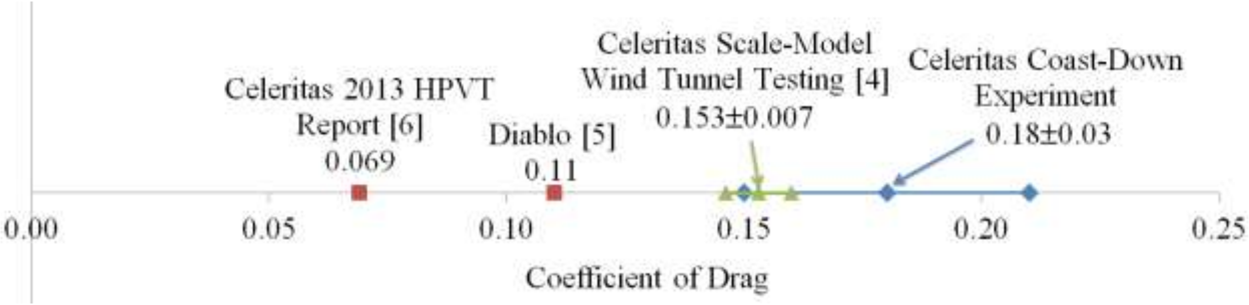

Figure 8: Resultant C_d with Other Relevant Values

Our value of 0.18±0.03 overlaps the result of another experiment on a scale-model of Celeritas placed in a wind tunnel [4], giving us confidence in our result. Furthermore, our total uncertainty of 16% meets our goal of under 25% and enables us to make definite conclusions. Our C_d value is significantly different than the C_d value of the Diablo (0.110) and what has previously been reported for Celeritas by the HPVT (0.069). This allows us to conclude that the SolidWorks estimate of C_d that the HPVT reports for Celeritas is not accurate to the physical vehicle. The actual C_d is at least twice as large as what HPVT reports. We can also reject the claim that Celeritas has a C_d that places it among the world's most aerodynamic vehicles.

Within systematic uncertainty, uncertainty in frontal area was the largest contributor. It had the largest relative uncertainty of all the measurands mostly due to the conservative approximation used to calculate it (see Appendices A and B). If uncertainty in frontal area were scaled down by a factor of ten, the resulting systematic uncertainty would be reduced by 16% and we would be able to report our resultant as 0.18±0.02. One method of determining area with higher certainty would be to photograph Celeritas in front of a grid with a fine mesh size and count the filled-in squares. Another would be to measure the deviances from the SolidWorks model to the final vehicle that are caused by manufacturing methods.

Recommendations

This experiment could be extended to any of the Rose-Hulman HPVs. The vehicles could not be directly compared with an uncertainty of 16% because their C_d uncertainties would most likely overlap. However, the resultant drag coefficients for each vehicle could be compared to what has been estimated for them via SolidWorks Simulations. This would allow the team to determine which simulation settings produce the most accurate results.

We assumed in our experiment that the vehicle traveled in an upright position. For a coast-down test where the rider is not pedaling, this is a good assumption. However, the vehicle does significantly lean from side to side when the rider is pedaling. Further testing could quantify this wobble with accelerometers and examine its effect on C_d.

Our analysis was constructed to determine C_d, but it could be adapted to determine rolling resistance coefficient f_r as well. The testing procedure would remain the same, and both parameters could be determined by the curve-fit. Our uncertainty analysis would need to be extended to include a resultant f_r.

References

[1] D. M. Smiadak, "Drag Coefficient of a Sphere," 8 July 2008. [Online]. Available: http://claymore.engineer.gvsu.edu/~smiadakd/EGR365-Lab8.pdf. [Accessed September 2013].

[2] J. A. DeMoss, "Drag Measurements on an Ellipsoidal Body," 21 August 2007. [Online]. Available: http://scholar.lib.vt.edu/theses/available/etd-09032007-103809/unrestricted/DeMoss_Masters_Thesis_Final.pdf. [Accessed September 2013].

[3] B. Jeffrey C. Stroman, "Aerodynamic Drag Coefficients of a Variety of Electrical Conductors," May 1997. [Online]. Available: http://repositories.tdl.org/ttu-ir/bitstream/handle/2346/18671/31295011762241.pdf?sequence=1 . [Accessed September 2013].

[4] Z. Ernst, D. Robertson, J. Walters, P. Woolfenden, “Measuring the Drag Area of a Human Powered Vehicle,” 2013. Academic paper at Rose-Hulman Institute of Technology.

[5] J. Lafford , “A Study Of Aerodynamic Drag On Faired HPV's,” 2002. [Online]. Available: http://www.legslarry.beerdrinkers.co.uk/tech/AeroDrag.htm

[6] Rose-Hulman Human Powered Vehicle Team, “2013 ASME East Coast HPV Challenge Report: Celeritas,” March 25, 2013. [Online] Available: http://hpvt.rose-hulman.edu/design-reports/2013/2013_Rose-Hulman.pdf

[7] Jeremy J. Worm P.E., Drew Dosson Brennan, Mr. Zeit T. Cai, "Experimental Studies in Ground Vehicle Coast-Down Testing," 2012. [Online]. Available: www.asee.org/public/conferences/8/papers/5030/download. [Accessed September 2013].

[8] "Determining Frontal Area of a Solid Model in Solid Works," [Online]. Available: http://fac-web.spsu.edu/met/kfleming/Determining%20Frontal%20Area.pdf. [Accessed September 2013].

[9] "Road Load Measurement and Dynamometer Simulation Using Coast Down Techniques," SAE International, 2010.

Appendix A—Uncertainty in Measurands

The systematic uncertainty in each measurand, x, (excluding velocity) can be determined by

$$w_{x,sys}{}^2 = w_{x,acc}{}^2 + w_{x,read}{}^2. \tag{A1}$$

The uncertainty values for the Royal 400 lb scale and the Kestrel 3500 Pocket Weather Meter originate from specification sheets found in the Rose-Hulman ME supply room. The sheets provide accuracies for both devices.

There is no available accuracy information on the router used to generate the fairing molds for Celeritas. The appropriate Rose-Hulman technician reported the router to be accurate to within 0.13 cm. To attain a conservative estimate for the uncertainty due to frontal area, we first assumed that the frontal area is a square. If the lengths of the sides of the square vary by as much as 2 cm, the resulting area change is 0.023 m^2. Given the router's precision, this 2 cm variation is a generous allotment for uncertainty in the frontal area. This analysis is demonstrated in Figure A1.

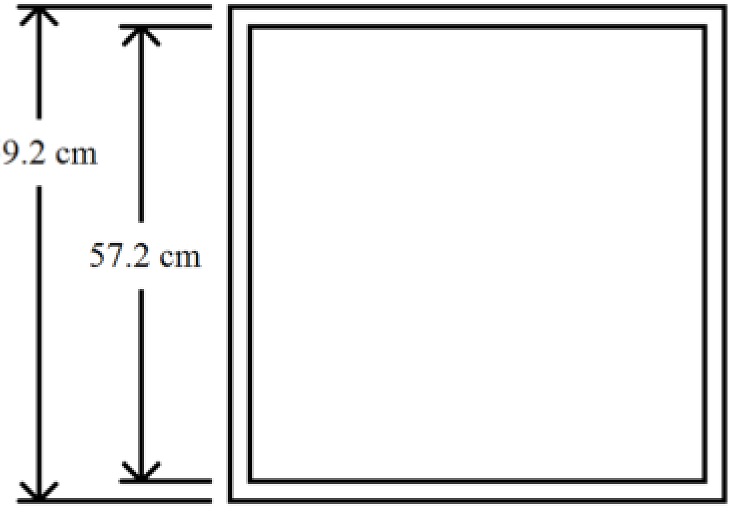

Figure A1: Representation of uncertainty analysis for frontal area

Systematic uncertainty in velocity is

$$w_{V,sys}{}^2 = \left(\frac{V_{meas}}{C}\right)^2 \left(2w_{C,read}{}^2\right) + \left(\frac{V_{meas}{}^2}{CF}\right)^2 w_{N_{counts},sys}{}^2. \tag{A2}$$

Garmin would not provide complete information on the accuracy of the Garmin Edge 500. However, wheel circumference was an input, and so it was assumed that the sensor operated by multiplying number of revolutions per time period by the circumference. Because a tape measure was used to determine the wheel circumferences, its readability was used in place of accuracy for the calculation of systematic uncertainty in velocity. The terms C and F refer to wheel circumference and frequency of the Garmin's timer, respectively. The term $w_{N_{counts},sys}$ refers to the uncertainty in the number of counts made by the Garmin. V_{meas} represents mean velocity and $w_{C,read}$ is the readability of the tape measure. Entering the following shakedown values into (A2) yields (A3).

$$w_{N_{counts},sys} = 0.5$$
$$C = 1.28m$$
$$F = 1024Hz$$
$$w_{C,read} = 1.5mm$$

$$w_{V,sys} = \sqrt{(2.74 \times 10^{-6})V_{meas}{}^{2} + (1.46 \times 10^{-7})V_{meas}{}^{4}} \tag{A3}$$

Our method of incorporating uncertainty in velocity is illustrated in the following example. Consider a first case with three points (x, y)=(1,1), (2,4), and (3,3), each with an uncertainty of 1 in y, that are being curve-fit by a line of the form $y = mx$. The least-squares regression determines the m value that minimizes the sum of the squares of the residuals. In this example, this gives an m value of 1.29 and a maximum residual of 1.43. The maximum residual determines linearity of velocity about the curve-fit. For our experiment, this linearity is root-sum-squared with random uncertainty to incorporate uncertainty in velocity into total uncertainty in C_d.

Next, consider the same points, but with (2,4) having an uncertainty of 3 in y. Because of its relatively higher uncertainty, the point is less important than the others for the curve-fit to pass directly through. The curve-fit adjusts down to come closer to the points known with higher certainty, giving an m value of 1.09 and a maximum residual of 1.81. The maximum residual grows from the first case because the curve-fit attaches less weight to the deviant point, increasing its distance from the regression line. For our experiment, linearity and the total uncertainty in C_d increase accordingly.

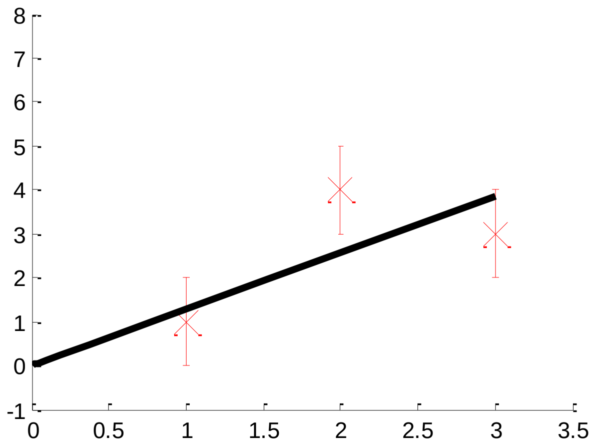

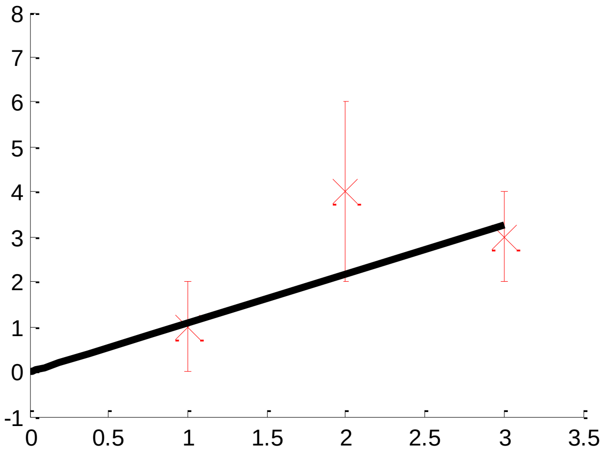

Figure A2: Points with curve-fits for Cases 1 and 2

Appendix B—Measurand Values

Measurand	Value	Relative Uncertainty (%)	Sources of Uncertainty	Sensor
Temperature	16.20 °C	6.2	Accuracy and readability	Kestrel Pocket Weather Meter 3500
Pressure	99.59 kPa	0.2	Accuracy and readability	Kestrel Pocket Weather Meter 3500
Individual Wheel Mass	1.24 kg	0.2	Readability and linearity	Acculab Econ 4100 g Scale
Vehicle and Rider Mass	104.60 kg	1.2	Accuracy and readability	Royal 400 lb Scale
Area	0.35 m^2	6.9	Assuming square model (Appendix A)	Square approximation
Parallel Wind Speed	0.0-0.7 mph	50%	Accuracy and readability	Kestrel Pocket Weather Meter 3500 and 2500
Vehicle Speed	11.4-34.2 mph	0.2-0.6	Accuracy and readability	Garmin Edge 500

Appendix C—Illustration of Simulation

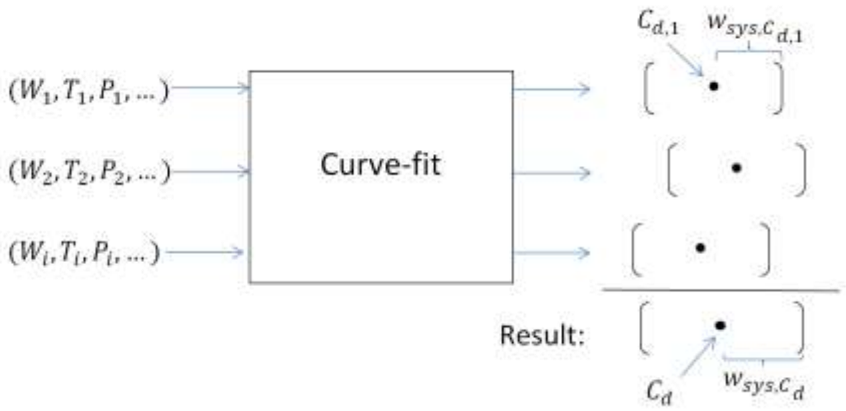

Figure C1: Curve-fit using simulated sets of measurand values

The curve-fit operation takes as input all the measurands values. It outputs one value of C_d and its respective systematic uncertainty. To factor in the uncertainty in measurands in our experiment, we simulated 500 values of each measurand. The values were normally distributed about the measured value with a standard deviation of the measurand uncertainty (i.e., $W_1, W_2, \ldots, W_{500}$ have a mean of the measured value of W and a standard deviation of $w_{sys,W}$.) The 500 sets of measurands were passed into the curve-fit, and 500 slightly different values for C_d and w_{sys,C_d}. The mean of these 500 $C_{d,i}$ values of C_d was our reported resultant, and our reported w_{sys,C_d} was large enough to capture 95% of the 500 $w_{sys,C_{d,i}}$ values.

Appendix D—Modifications Between Shakedown and Final Testing

The most significant change to our experimental procedure was in the slope requirements for our specific coast-down test. Because the HPV is significantly lighter and more aerodynamic than a full size vehicle, the allowable elevation change is ten times smaller than that specified in the SAE standard. We used a taxiway at the Terre Haute International Airport for our test. Only a fraction of the taxiway had an acceptable elevation change, so we marked this section and only recorded data within this stretch. This shortened the range of the velocity data we were able to collect, but the noise factor of the slope was removed.

In addition, we took wind speed data both parallel and perpendicular to motion. The perpendicular component determined if we met the maximum crosswind requirements posed by the SAE standard. Then, rather than assuming the headwind was negligible, we adjusted the vehicle speed data according to the wind speeds. This is an acceptable procedure because aerodynamic drag force is dependent on the speed of the vehicle relative to local air speed.

We had originally decided that atmospheric temperature and pressure could be measured at the beginning of the trials and then again after all data was recorded. After our shakedown, we decided that we should measure the atmospheric temperature and pressure before each trial. We also checked the vehicle’s tire pressure more frequently to have more confidence in our assumption that tire pressure was constant.

Appendix C

Measuring the Drag Area of a Human Powered Vehicle

ME421-04 Group 5

Zach Ernst
Drew Robertson
Jeremy Walters
Patrick Woolfenden

Mechanical Engineering Laboratory

Dr. Michael Moorhead

November 15, 2013

Introduction:

The Rose-Hulman Powered Vehicle Team (HPVT) builds an aerodynamic bicycle to compete in the ASME competition each year. The key to producing the fastest vehicle is to improve the vehicle's aerodynamics and minimize the drag force. Drag force is part of the drag equation, Equation 1, and is derived from fluid dynamics and dimensional analysis.

$$F_D = \frac{1}{2}\rho V^2 C_D A \tag{1}$$

Drag area, $C_D A$, is directly proportional to the drag force, F_D, for all velocities, V. Minimizing the drag area is the easiest way to reduce a vehicles drag force and increase top speed. The coefficient of drag, C_D, and the characteristic area, A, make up the drag area. Each vehicle design has its own coefficient of drag and its own area which will create a unique drag area. Drag area will be used because it captures both C_D and A for each vehicle and it shows which design will have the lowest drag force and corresponding highest top speed.

To further increase the top speed of a human powered vehicle (HPV) a better estimate of the drag area is necessary to determine the effects of different aerodynamic features and which shape has the lowest drag force. This project seeks to create an experiment that will measure the drag area on a HPV to analyze different vehicle body designs and the aerodynamic impact of additional features like mirrors and wheel covers.

In order for the results of the test to be meaningful, the experiment will have to determine the drag area with enough accuracy to show the impact of different aerodynamic features and vehicle shapes. To determine the necessary accuracy, the drag areas for several HPV bodies were determined with computational fluid dynamics (CFD) and compared in Figure 18.

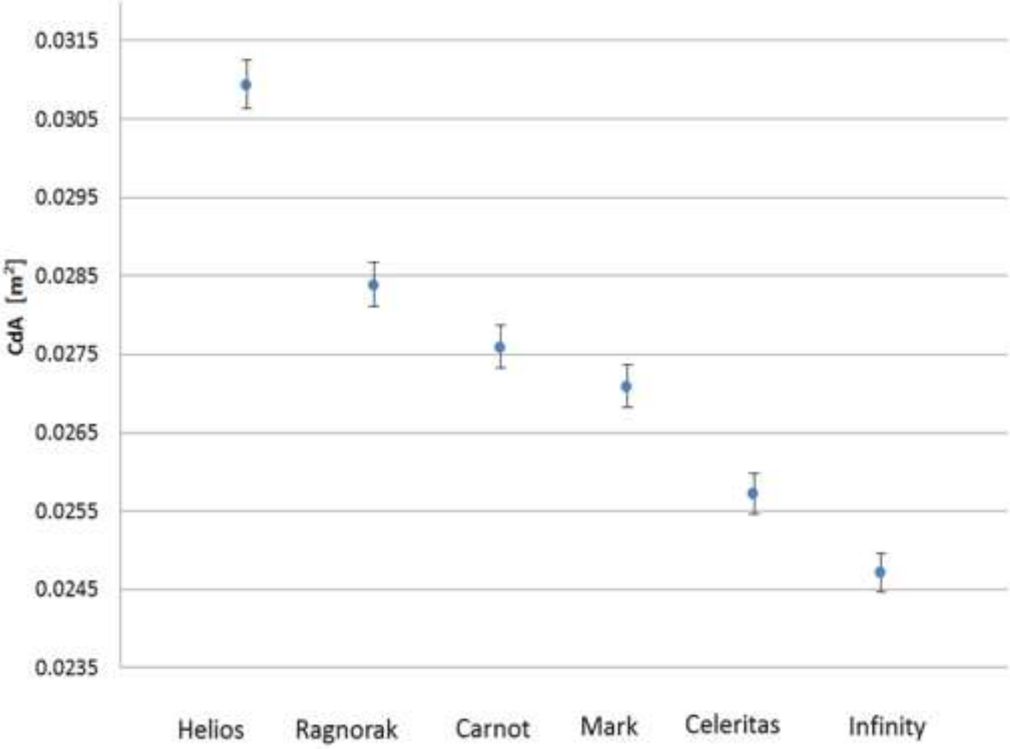

Figure 18: Expected $\boldsymbol{C_D A}$ *values from SolidWorks flow simulation for full size bodies with 1% error bars.*

Almost all of the HPVT's previous vehicles can be differentiated when the relative uncertainty is at or below 1% as shown graphically with the error bars in Figure 1. Unfortunately considering that random uncertainty on a wind tunnel is about 1% based on previous experience [1], a 1% total relative uncertainty is not large enough. A 2% target uncertainty will be able to distinguish half of the previous HPV models and will allow for more random and systematic uncertainty. The experimental setup could be able help determine the effects of various aerodynamic features, like vortex generators and wheel covers, on the overall drag area of the vehicle. If the impact of these features has less than a 2% change in the total drag area, our experimental setup would not be able to distinguish the effects and it is arguable that the aerodynamic feature has little impact on the vehicles aerodynamics and is not worth pursuing.

Design Selection

The drag area can be found for an actual vehicle or a scaled model of an HPV. The actual vehicle has the advantage of producing the exact drag force because it includes every detail of the vehicle, but it is difficult to test because of its size. A scaled model of an HPV can be tested in a wind tunnel but will not have the same drag area as the full scale vehicle, because it is a simplified version without door jams, mirrors, and other features that affect the vehicles drag area.

Research done by Crewer and Passmore indicates that a coastdown test can be used to estimate $C_D A$ for any vehicle [2]. A coastdown test involves bringing the vehicle up to speed, putting the vehicle in neutral, recording the velocity as it decelerates, and fitting a model to the velocity-time curve. Because the rolling resistance of the vehicle would have to be accounted for and large uncertainties develop when fitting a model to a velocity versus time graph, coastdown testing was deemed unsuitable for finding the drag area of an HPV.

Another potential method for finding the drag area would be to use a capture carry system where an HPV would be mounted to an automobile and drag force would be measured while the automobile is driven at constant speed down a smooth road. Unfortunately this setup was determined to have a high uncertainty because of the limitations of available anemometers and the uncertainty in the road surface.

Wind tunnel testing has a lower predicted uncertainty in drag area than full scale testing because of the controlled environment with less random uncertainty and direct measurands [3]. Even though scale models would not have all the features of the final vehicles they would still provide meaningful results for comparing vehicle shapes and features as long as the Reynolds numbers for the model and full scale are similar.

Reynolds number is the ratio of inertial forces to viscous forces in a variety of fluid flows and is defined in Equation 2 for external flow.

$$Re = \frac{\rho v L}{\mu} \tag{2}$$

Since the working fluid is air in both full-scale and small-scale testing, ρ, density, and μ, dynamic viscosity, will be the same. The only parameters that can change to match Reynolds number are L, the characteristic length, and v, the wind tunnel velocity. The wind tunnel model's Reynolds number is limited by the maximum velocity of the air and the size of the model.

HPVs have been tested as 50% scale models in wind tunnels by Royal Melbourne Institute of Technology (RMIT), but Rose-Hulman's wind tunnels cannot test anything near that large [4]. The models for this experiment would have to be scaled down to at least 12.5% to meet the blockage area rule of thumb for wind tunnels. Blockage rate is the ratio of the frontal area of the model and the cross sectional area of the wind tunnel test section.

$$BlockageRate = \frac{Area_{Frontal,model}}{Area_{Frontal,Test\ Section}} \leq 5\% \tag{3}$$

Keeping the blockage rate under 5% helps insures that the flow stays incompressible as it passes the model and that the fan can continue to pull air through the wind tunnel.

The velocity that the models can be tested at is limited by the capabilities of the wind tunnel's motor and fan. The large wind tunnel in Rose-Hulman's Rotz lab is capable of producing wind speeds up to 67 m/s in the test section.

When using the wind tunnels maximum velocity and the largest model size available with a 5% blockage rate the Reynolds numbers are on the same order of magnitude, but the full scale model's Reynolds number is about three times larger than that of the scaled down model.

Table 16: Maximum Reynolds number for the scaled down model compared to the full sized HPV

$\boldsymbol{L\ [in]}$	$\boldsymbol{L\ [m]}$	$\boldsymbol{U\ \left[\frac{m}{s}\right]}$	$\boldsymbol{v\ \left[\frac{m^2}{s}\right]}$	$\boldsymbol{Reynolds\ Number}$
96	2.4384	20	0.00001568	3.11E+06
12	0.3048	67	0.00001568	1.30E+06

In this experiment, a 1/8th scale model of an HPV well be tested near the maximum velocity for the Rose-Hulman large wind tunnel. Even though the Reynolds numbers do not match perfectly they are very close and C_D is unlikely to vary much as shown by the airfoil in Figure 19. An HPV can be approximated as an airfoil, because they are both streamlined bodies. From the figure C_D is nearly constant between 1.3x10^6 and 3.1x10^6.

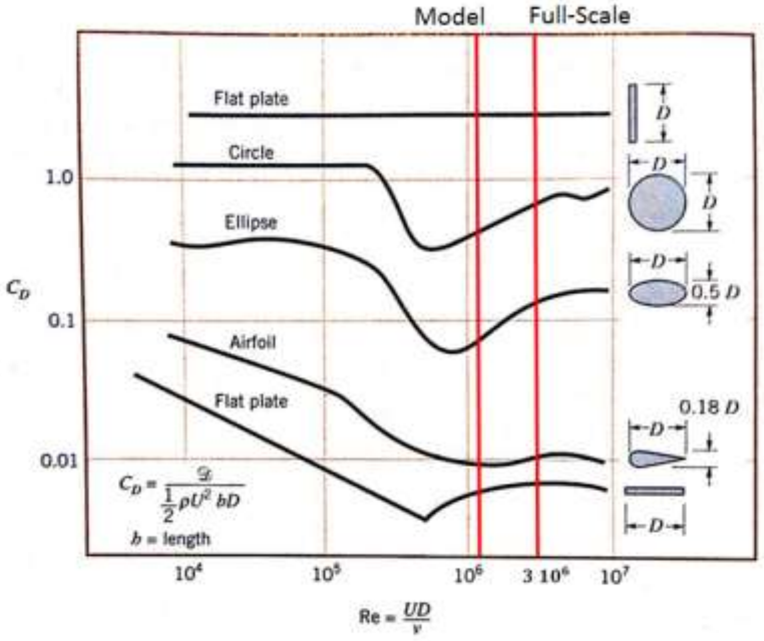

Figure 19: The Reynolds numbers for the model and full scale HPVs are shown as red lines in this plot of $\boldsymbol{C_D}$ for different shapes as a function of Reynolds number. [5]

A sanity check using Solidworks Flow Simulation agreed with Figure 19 and showed that $C_D A$ is nearly the same at this lower Reynolds number for the full-scale HPV.

From the available testing apparatus designs, wind tunnel testing with eighth scale models was chosen as the best method to test for the drag area of a HPV, because initial uncertainty calculations showed that the wind tunnel could measure drag area within the 2% relative uncertainty goal.

Design

The experimental design will test a scale model of the HPV inside a wind tunnel using the setup in the figure below.

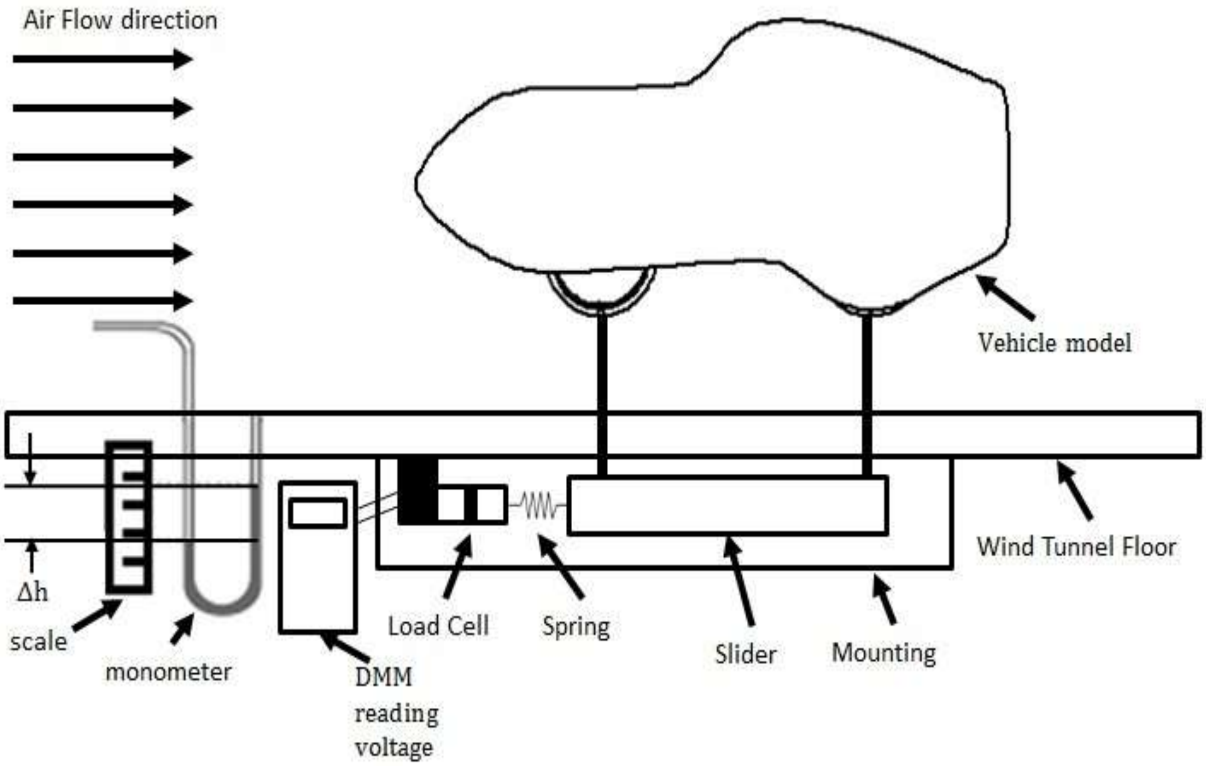

Figure 20: The experimental setup in the wind tunnel will measure the drag force with a flat plate load cell.

The model is mounted on a low-friction slider by two cylindrical rods and positioned inside the wind tunnel test segment. The drag force on the model is balanced by the load cell in tension. A spring is used to protect the load cell by limiting the displacement of the model. Force data from the load cell is read using a digital multimeter and velocity is measured by a change in fluid height on a manometer board. The measured voltage from the digital multimeter will be converted to force through a calibration equation for the load cell. In a wind tunnel velocity is measured by taking the difference between dynamic and static pressure in a manometer tube.

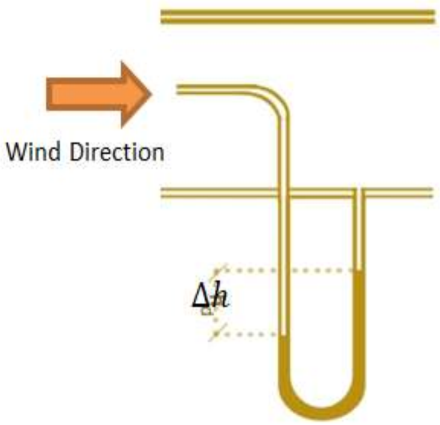

Figure 21: Dynamic pressure is the difference between stagnation and static pressure and can be measured by a change in fluid height. [6]

The dynamic pressure can be represented as:

$$\frac{1}{2}\rho V^2 = \rho_l g(h_{stag} - h_{static}) \tag{4}$$

Where h_{stag} is the height of the fluid in the tube hooked up to the stagnation pressure and h_{static} is the height of the fluid in the tube hooked up to the static pressure tube. The data reduction equation for this experiment, Equation 5, is derived from Equations 1 and 4.

$$C_D A = \frac{F}{\rho_l g(h_{stag} - h_{static})} \tag{5}$$

The drag force, F, h_{stag}, and h_{static} are the only measurands in this experiments. Gravity, g, is considered constant because the testing is taking place at the same elevation during testing and it takes a large elevation change for gravity to change. The density of the manometer fluid, ρ_l, is assumed to be constant as well because the density of the fluid has a relatively small impact on the final result and it takes a large temperature difference to change the density. There is little chance of large temperature differences, because all of the testing will be done at room temperature.

Measurement Device Selection

To measure the drag force a load cell will be used to measure the force, because there are available load cells with appropriate characteristics to meet the 2% uncertainty goal. Most models that are tested in a wind tunnel use a load cell called a sting balance to measure the drag, lift, and yaw of the sample. The sting balance has a measurable range of 0 to 44.5 N. Because there is no formal documentation on the uncertainty of the sting balance, a calibration is usually performed to find the uncertainty. To approximate this uncertainty it was assumed that the sting balance had similar accuracies as other linear load cells. Assuming the uncertainty was equal to 0.25% of the full scale value, the sting balance was found to have relative uncertainty of 13.5% when measuring the drag force on an eighth scale HPV with an estimated 0.82 N drag force. Because of this large uncertainty a smaller load cell, one with a 0 to 1.13 N range and 0.35% relative uncertainty, was used instead of the sting balance. The accuracy of both sensors can be found using Equation 6. The $LoadCell_{Max}$is the maximum force of the load cell's range, and $\omega_{\mathrm{F,acc}}$ is the accuracy of the sensor.

$$\omega_{F,acc}{}^2 = (.0025 * LoadCell_{Max})^2 \tag{6}$$

The process for determining the sensors used was to input their specifications into an uncertainty budget and calculate a percent error with a theoretical value for $C_D A$ and an assumed random uncertainty of 1.5%. The force will be measured using a digital multimeter and a linear load cell with a maximum load of 1.13N. The heights of the fluids will be read off of a manometer board in tenths of an inch. These sensors were chosen to limit the uncertainty below the target 1% threshold for systematic uncertainty.

Table 17: Sensors were chosen to minimize systematic uncertainty.

Measurand	Sensor	Scale	$\boldsymbol{\omega_{sys}}$
$\boldsymbol{F}$	Omega LCL-113G	0 - 1130 mN	2.9 mN
$\boldsymbol{h_{stag}}$	Manometer Board	0 – 356 mm	1.8 mm
$\boldsymbol{h_{static}}$	Manometer Board	0 – 356 mm	1.8 mm

Using Equation 5, the equation for the systematic uncertainty of $C_D A$ is found to be:

$$\omega_{\mathrm{C_DA}}{}^2 = \left(\frac{\partial \mathrm{C_DA}}{\partial \mathrm{F}}\right)^2 \omega_{\mathrm{F}}{}^2 + \left(\frac{\partial \mathrm{C_DA}}{\partial \mathrm{h_{stag}}}\right)^2 \omega_{\mathrm{h_{stag}}}{}^2 + \left(\frac{\partial \mathrm{C_DA}}{\partial \mathrm{h_{static}}}\right)^2 \omega_{\mathrm{h_{static}}}{}^2 + \omega_{\mathrm{C_DA,rand}}{}^2 \tag{7}$$

After performing a calibration test for the load cell specified in Table 17 it was found that the specified load cell had an uncertainty that was sixteen times greater the predicted value. This finding is discussed further in the Test and Refine section in Appendix[C] of this document, but the increased uncertainty in force increased the overall uncertainty beyond the original 2% uncertainty goal as shown in Table 18.

Table 18: The uncertainty budget for the experimental setup predicted the uncertainty will be 6%.

Parameter	Value	Uncertainty	Relative Uncertainty	RSSC (%)	UPC (%)
$\mathbf{C_d A_{rand}}$			1.50%	1.50%	5.86%
F [mN]	825	48	5.84%	5.84%	88.92%
h_{stag} **[mm]**	205	1.8	0.74%	0.83%	1.81%
h_{static} **[mm]**	25	1.8	7.07%	0.83%	1.81%
$\mathbf{C_d A}$ **[cm²]**	4.69	± 0.29			
			Total:	6.14%	100.00%

This predicted uncertainty does not meet the original 2% target uncertainty goal, but it will still be able to detect differences in $C_D A$ between most models. To show the different models that can be tested with this setup under the full range of wind speeds the following design space was created.

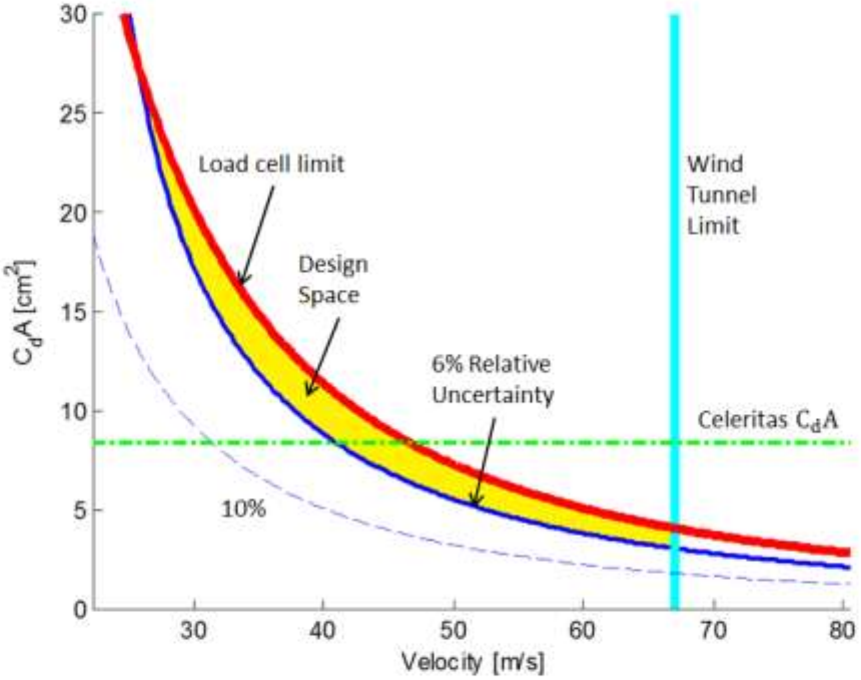

Figure 22: The design space for the proposed experiment with the expected $\boldsymbol{C_D A}$ *and the wind speed used during testing.*

The design space for the experiment set up illustrates the range of settings that will have less than 6% uncertainty in $C_D A$. The curved red line represents the maximum force that the load cell can take and the vertical cyan line represents the maximum speed of the wind tunnel. These are the ceilings to the experiment and require the design space to be below these values. The lower limit for the range of testable settings is determined by the desired amount of overall relative uncertainty. The solid blue line represents the lower limit for finding $C_D A$ within 6%, while the dashed line represents 10% relative uncertainty. The $C_D A$ from testing, 8.4 cm^2, for a 1/8th scale model of an HPV is shown as the dashed green line on the plot and is in between the maximum and minimum $C_D A$ values for 6% relative uncertainty, 27 cm^2 and 3 cm^2 respectively. The design space illustrates the level of uncertainty in $C_D A$ that can be expected for different models and the wind speed that is necessary to meet that level of uncertainty.

Experimental Method

Ten measurements for each model were taken over the course of two days and the models were tested in a randomized order to account for all forms of uncertainty. Data was recorded at 80% of the maximum velocity of the wind tunnel in order to minimize the variability in wind speed. The drag force of the posts was subtracted from the drag force of each of the models to find the experimental $C_D A$ values.

To check the accuracy of the experimental results, ten tests were run with a 0.9 inch diameter, by 4 inch long cylinder. These values were compared against the reported and accepted $C_D A$ values for a cylinder [7], and the theoretical results from CFD analysis.

Table 19: Cylinder $\boldsymbol{C_D A}$ validation for the experimental setup.

Method	$\boldsymbol{C_D A}$ $[\mathbf{cm}]^{\mathbf{2}}$	Uncertainty
Experimental	3.2 ± 0.4	11.11%
CFD Predicted	3.40	
Theoretical	3.31	

The average experimental drag area of the cylinder was lower than the theoretical value and the CFD predicted value but these values are included within the range of uncertainty. From the values in Table 4 it can be shown that the wind tunnel will produce values that are slightly lower than accepted but the experimental value will still capture the expected values within the uncertainty bounds.

Results

The final values of drag area for the Celeritas and Carnot HPV models are shown in Table 20 with their respective uncertainties. The full-scale drag area can be computed by multiplying the model drag area by 64, because the model is one eighth scale and is one sixty fourth of the full-scale area. The calculations used to find the uncertainties for the models and the control cylinder can be found in Appendix [B].

Table 20: Experimental relative uncertainty of drag area for both models was about 5%.

Model	Model $C_D A$ [cm^2]	Relative Uncertainty	Full-Scale $C_D A$ [m^2]	CFD $C_D A$ [m^2]
Carnot	9.4 ± 0.4	4.7%	$0.060 \pm .003$	0.028
Celeritas	8.3 ± 0.4	5.3%	$0.053 \pm .003$	0.026

The relative uncertainty was below 6%, because the load cell was near its full capacity. There was also lower random uncertainty, because the models had similar wheel bases and required minimal adjustment of test apparatus between tests. The uncertainties are low enough that the models are statistically different as shown in the figure below.

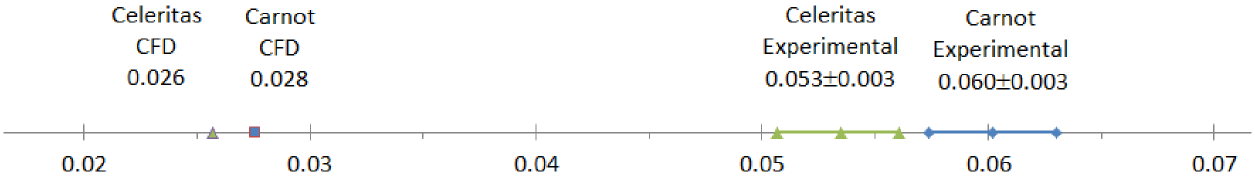

Figure 23: The Carnot and Celeritas models are distinguishable because their respective error bars do not cross.

The values of 0.060 m^2 and 0.053 m^2 for the full-scale drag area for the Carnot and Celeritas are higher than the CFD predicted values of 0.028 cm^2 and 0.026 cm^2. Some of this difference can be attributed to the error included in the subtraction of the apparatus's posts drag area and the differences in relative surface roughness between the full-scale CFD and the scale models. The difference in the relative roughness can be understood by looking at the effects of surface roughness on the drag coefficient of a flat plate as shown in Figure 24.

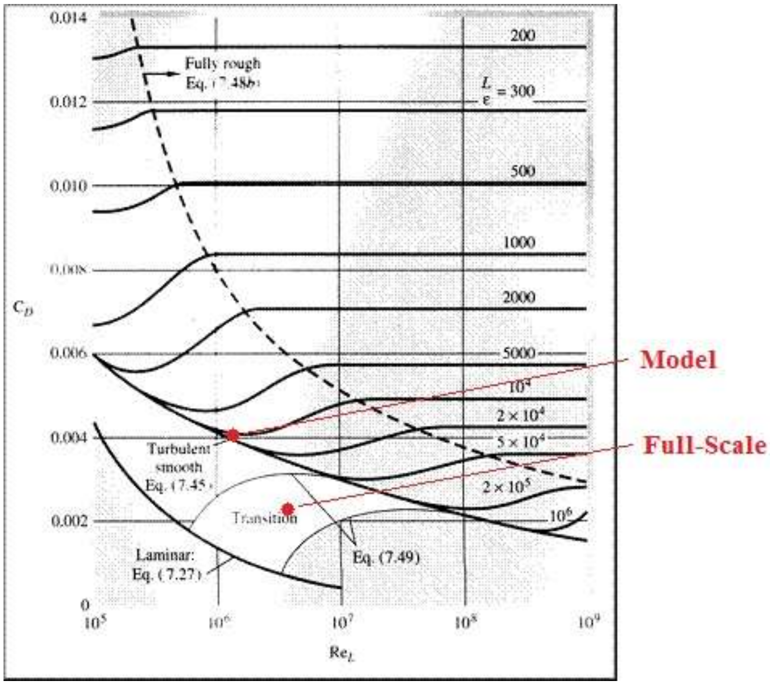

Figure 24: Effects of relative roughness on the drag coefficient of a flat plate [8].

If the full-scale and 1/8th scale HPV models can be assumed to have a similar dependence on relative roughness as a flat plate, the drag area will double for the scale model if it is the same absolute roughness as the full-scale vehicle. During preliminary testing of the models, a noticeable decrease in drag area was observed after the models were sanded to a finer finish. This preliminary testing and Figure 24 solidify the need to match the relative roughness between the full-scale HPV and the scale model in future testing to finding accurate drag area values.

The drag area approximation for the posts holding the model is another source of error in the final results. In future experiments a control object, like a cylinder, could be used as a method for finding the appropriate drag area for the posts. The analytical model would be updated until the experimental cylinder drag area matched the accepted drag area.

Conclusion

While the experimental and CFD values differ substantially, the importance is the difference between each model. The current experimental setup can detect differences between models as long as the same amount of the posts is exposed to the flow for each test and the apparatus does not have be removed from the wind tunnel when changing models. The CFD values show the Carnot has the higher drag area by 8%, and the experimental setup in the wind tunnel shows that the Carnot was 13% higher. Because both methods detected the difference between the two vehicles, it can be said that the Carnot has a higher drag area than the Celeritas.

This experiment produced a valuable addition to the Rose-Hulman HPVT tool chest. The design of the apparatus and appropriately selected sensors resulted in the ability to analyze the aerodynamics of different HPV shapes. Higher precision sensors for measuring the drag force and wind speed may be required in the future to better distinguish between smaller variations in features. But with the current setup and procedure, it was confirmed that the Celeritas has a lower drag area than the Carnot.

References:

[1] Robertson D., Harper M., McClintock , Bailey G., 2013, *Wind Tunnel Correction Factor*, Rose-Hulman Institute of Technology Measurements Lab

[2] Crewe, C., Passmore, M., Symonds, P., 1996, “Measurement of Formula One Car Drag Forces on the Test Track,” 2114-2120, Society of Automotive Engineers, Inc.

[3] Morris, M. and Post, S., 2010, “Force Balance Design for Educational Wind Tunnels,” ASEE AC-2010-393

[4] Alam, F., Chowdhury, H., Guillaume, E., Yang, J., Zimmer, G., 2013, “On-road and Wind Tunnel Aerodynamic Study of Human Powered Vehicles”, 473-478, Procedia Engineering 60 (2013)

[5] Munson B., Okiishi T., Huebsch W., Rothmayer A., 2013, *Foundation of Fluid Mechanics*, John Wiley & Sons, Inc., United States, Chap. 9.2, 6.9.

[6] Automation Wiki, 2010, “Pitot Tube,” from http://automationwiki.com/images/e/e2/Pitot_Tube.jpg

[7] Scott, J., 2005, “Drag of Cylinders & Cones,” from http://www.aerospaceweb.org/question/aerodynamics/q0231.shtml

[8] Chklovski, T., “Pointed-tip wings at low Reynolds,” from http://www.wfis.uni.lodz.pl/edu/Proposal.htm

Appendix [A]

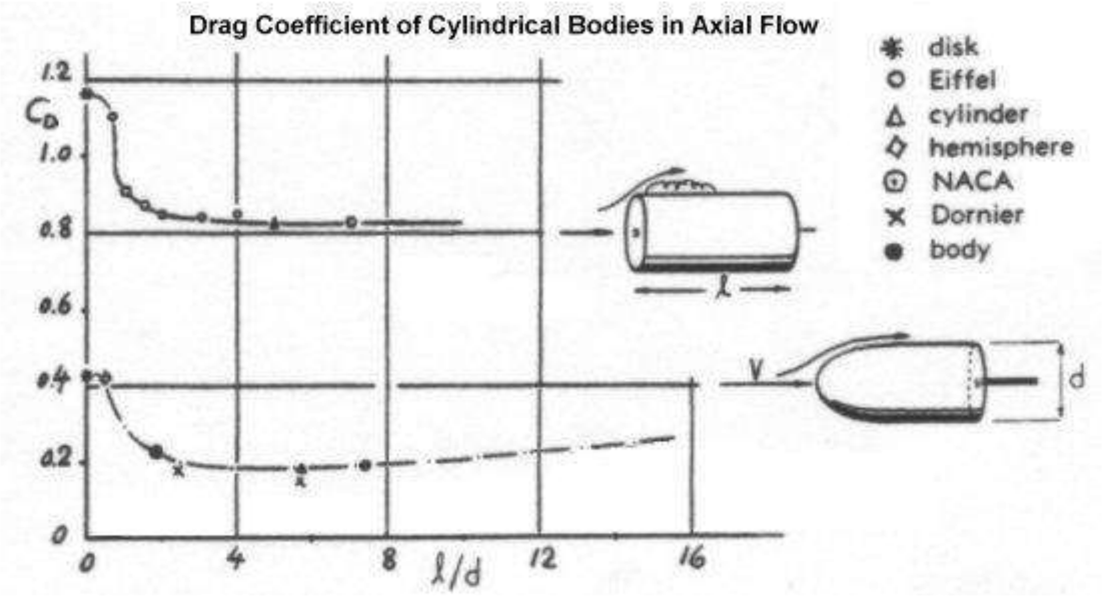

Figure 25: Drag coefficient chart for the prediction of the control cylinder's drag area [7].

Appendix [B]

Table 21: Control Cylinder Uncertainty Budget

Parameter	Representative Value	Uncertainty	Relative Uncertainty	UMF	RSSC (%)	UPC (%)
$C_D A_{,RAND}$			2.41%	1	2.41%	4.69%
$F\ [N]$	0.860	0.0482	5.60%	1.88	10.51%	89.49%
$h_{stag}\ [m]$	0.330	0.0018	0.54%	3.48	1.89%	2.91%
$h_{static}\ [m]$	0.152	0.0018	1.18%	1.61	1.89%	2.91%
$C_D A\ [cm^2]$	3.18			9.96	11.11%	100.00%

Table 22: Carnot's Final Uncertainty Table

Parameter	Representative Value	Uncertainty	Relative Uncertainty	UMF	RSSC (%)	UPC (%)
$C_D A_{,RAND}$			0.90%	1	0.90%	3.64%
$F\ [N]$	1.44	0.0482	3.34%	1.24	4.14%	77.20%
$h_{stag}\ [m]$	0.305	0.0018	0.59%	2.48	1.46%	9.58%
$h_{static}\ [m]$	0.152	0.0018	1.18%	1.24	1.46%	9.58%
$C_D A\ [cm^2]$	9.41			7.96	4.72%	100.00%

Table 23: Celeritas' Final Uncertainty Table

Parameter	Representative Value	Uncertainty	Relative Uncertainty	UMF	RSSC (%)	UPC (%)
$C_D A_{,RAND}$			1.18%	1	1.18%	5.0%
$F\ [N]$	1.31	0.0482	3.67%	1.27	4.67%	78.8%
$h_{stag}\ [m]$	0.305	0.0018	0.59%	2.54	1.50%	8.1%
$h_{static}\ [m]$	0.152	0.0018	1.18%	1.27	1.50%	8.1%
$C_D A\ [cm^2]$	8.36			8.08	5.26%	100.00%

Table 24: Full-Scale Captive Carry Uncertainty Budget

Parameter	Representative Value	Uncertainty	Relative uncertainty	UMF	RSSC (%)	UPC (%)
CdA_rand			2.00%	1	2.00%	38.43%
k [N/m]	43.7814085	0.3	0.69%	1	0.69%	4.51%
x [m]	0.406400813	0.001587503	0.39%	1	0.39%	1.47%
T [K]	300	1	0.33%	1	0.33%	1.07%
P [Kpa]	101	0.1	0.10%	1	0.10%	0.09%
V [m/s]	25	0.297542014	1.19%	2	2.38%	54.43%
R [KJ/kg*K]	0.287	0	0.00%	1	0.00%	0.00%
CdA [m^2]	0.048537349			8	3.23%	100.00%

Appendix [C]

Shakedown and Refinement

A calibration was performed on the load cell by hanging weights from it, creating a linear curve fit between voltage and force, and determining the maximum deviation of the actual voltage reading to the predicted voltage reading.

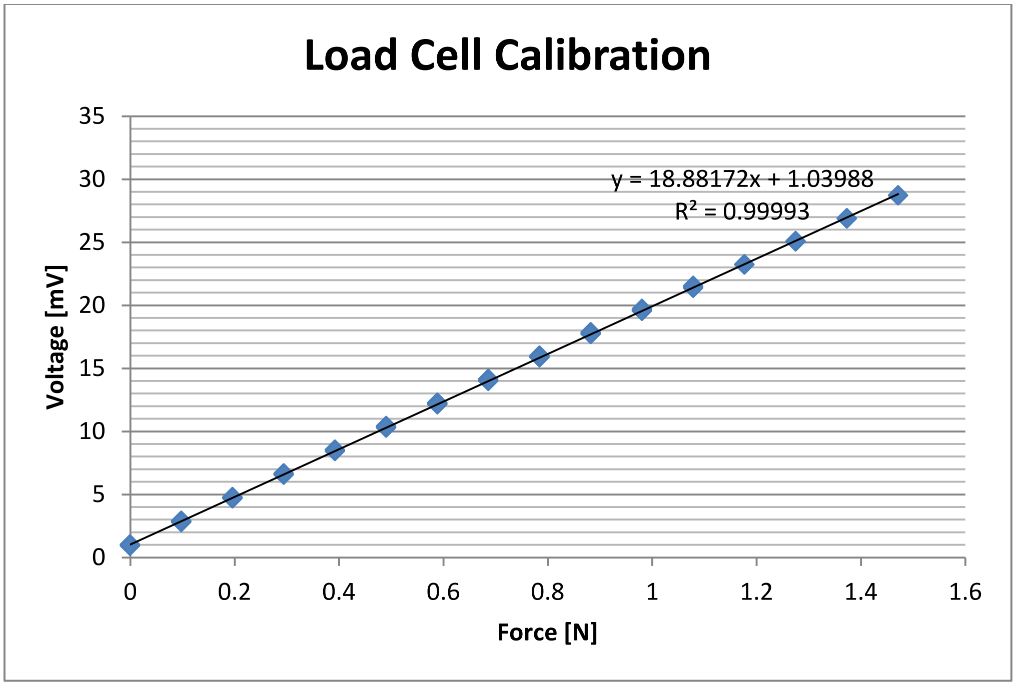

Figure 26: The cell was calibrated by hanging different masses and measuring the output voltage from the DMM.

The maximum deviation of the load cell during this calibration was 0.048 N. Unfortunately this uncertainty was 16 times higher than the predicted value of 0.0029 N and increased our overall uncertainty in drag area.

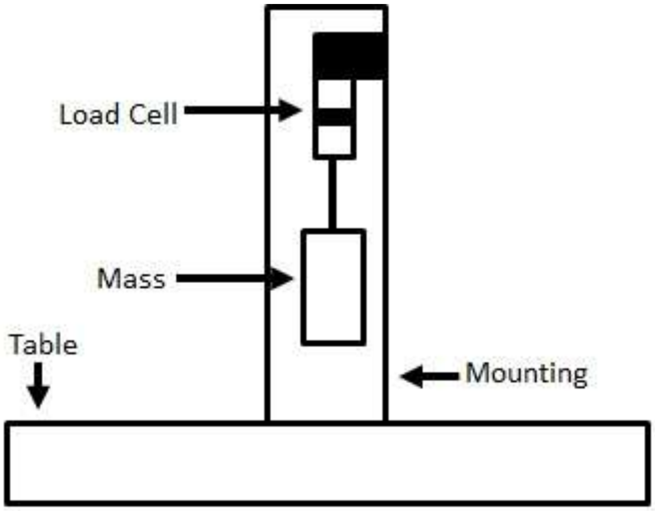

Figure 27: The load cell was calibrated by hanging weights from it and measuring the voltage output.

Initial installation of the apparatus into the wind tunnel required modifying the design in order to have clearance from the sting balance, which could not be fully removed. Additionally, the first trials with the cylinder demonstrated that friction between the bearings and the tracks was causing the apparatus to stick. This was solved by improving the finish on the tracks by wet sanding them with 1000 grit sandpaper.

The shakedown test was designed to test the apparatus and experimental procedure and to determine if they will produce credible results. To this end, the shakedown was performed with a cylinder to be able to compare the measured value of the drag area to a published theoretical value.

The initial results were consistently higher than the predicted values. The higher drag area was due to the drag force produced by the posts holding the model in the wind tunnel, so a set of trials to find the drag of the apparatus posts was conducted. For future trials, the drag area of the exposed posts will be subtracted using the formula:

$$C_D A_{wp} = \frac{C_D A_{posts}}{l(l - l_m)} \tag{8}$$

$C_D A_{posts}$ is the drag area of the posts alone, l is the length of the posts, l_m is the length of the posts covered by the model, and $C_D A_{wp}$ is the drag area of the exposed posts. This weighted average provides an approximation of the drag from the posts with the model attached and was subtracted from all of the drag area calculations.

Ten tests were performed with the cylinder, while randomly re-installing the apparatus and turning off the wind tunnel between each trial. This shakedown yielded experimental results of:

Table 25: The experimental cylinder control test versus the analytical prediction.

	$C_D A$ cm^2
Theoretical	3.31
Experimental	3.20 ± 0.4

The results of the shakedown demonstrate that the experimental setup measures drag area at about the same level as expected values. With the shakedown, a better estimate of the random uncertainty was found and used in Table 3. The largest source of random uncertainty was removing and replacing the entire apparatus on the wind tunnel. When testing the HPV models there was greater care given in placing the apparatus and trying to make as few adjustments as possible.

Appendix [D] – Measurements Lab

Grant Bailey, Matthew Harper, Drew Robertson, Brian McClintock
ME321-02 Measurement Systems
Dr. Haan
3/25/2013

Experiment 1 Report: Wind Tunnel Correction Factor

Introduction

The objective for Experiment 1 was to calculate the wind tunnel correction factor and its associated uncertainty for wind tunnel 1 in the Rotz Lab. Another objective was to investigate the possibility of a correlation between wind speed and the tunnel correction factor. The tunnel correction factor serves two purposes. It increases accuracy of wind tunnel testing, and allows the user to calculate the dynamic pressure at the testing site without the necessity of a Pitot tube. The correction factor accounts for the drop in the dynamic pressure from the entrance of the wind tunnel to the testing site. Dynamic pressure is the sum of the static and stagnation pressures. Static pressure is defined as the pressure of a fluid on a body when the body is at rest relative to the fluid. Stagnation pressure is found at a point where the fluid is not moving or stagnant, like at the tip of a Pitot tube. The drop in dynamic pressure between the entrance to the tunnel and the testing site is caused by friction between the fluid, air, and the wall of the wind tunnel. At the conclusion of the experiment the average tunnel correction factor was compared with one provided by Dr. Mayhew.

Experimental setup

As air flows through the wind tunnel, the stagnation and static pressures for the inside the test chamber, as well as the tunnel static pressure at the entrance to the testing chamber are obtained. A Pitot tube was used to measure the stagnation and static pressures inside the testing chamber. The air speed through the chamber was varied and the Pitot tube was readjusted for each measurement to account for random uncertainty. Measurements were done on multiple days to account for additional random uncertainty in atmospheric pressure, temperature, and humidity. The data obtained is available in Appendix A, Table 1.

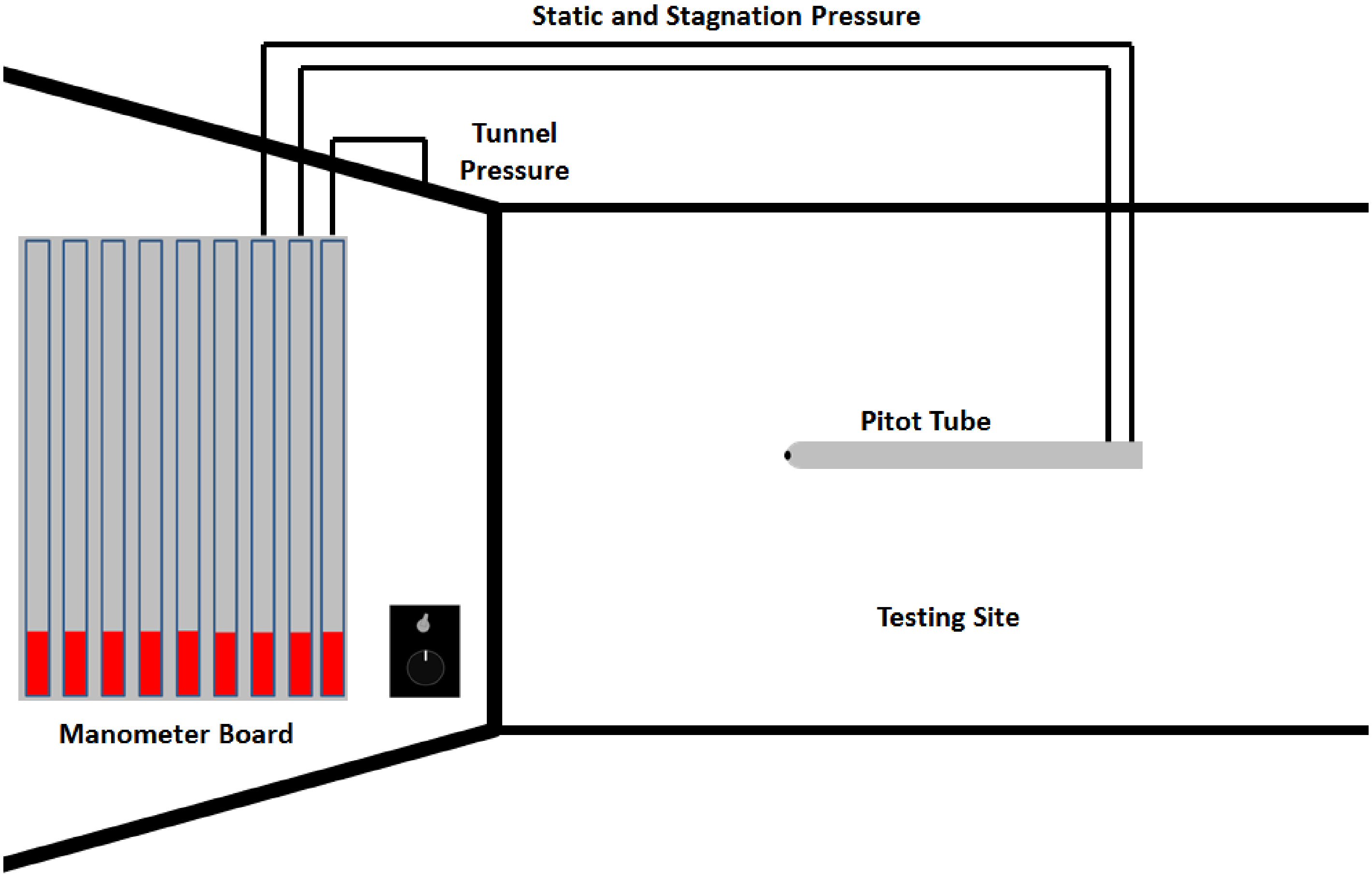

Figure 28: Experimental Setup

Figure 29: Hookups for the pressure tubes on manometer board

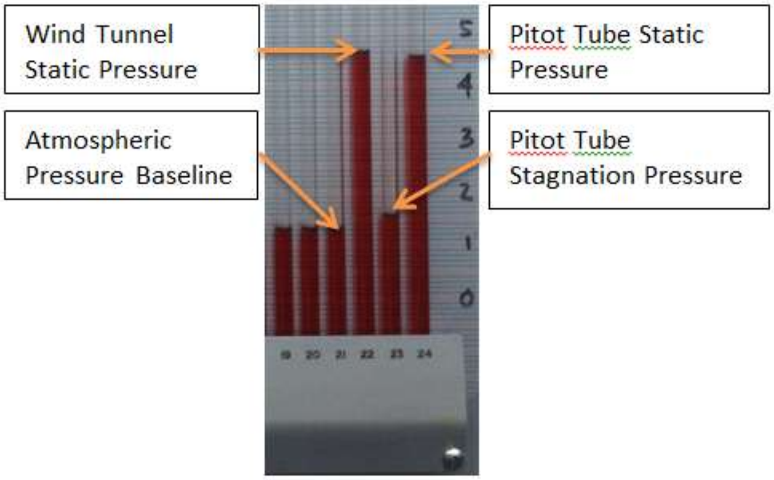

Figure 30: Manometer pressure readings

Method of Analysis

The correction factor, shown in Equation 1, is calculated by the ratio between the dynamic pressure of the wind tunnel, compared to the Pitot tube dynamic pressure. Dynamic pressure is the difference between the static pressure and the stagnation pressure. These pressures are recorded as heights of fluid, which are measured from the monometer board. The dynamic pressure of the Pitot tube is shown in Equation 2. The stagnation pressure for the tunnel is the pressure of air inside the room, since the air outside the wind tunnel isn’t moving.

R- correction factor
Q_{pitot}- dynamic pressure of Pitot tube
Q_{tunnel}- dynamic pressure of tunnel
P_{stag}- stagnation pressure of Pitot tube
P_{stat}- static pressure of Pitot tube
P_{atm}- atmospheric pressure of room
P_{tunnel}- static pressure in tunnel
ρ- density of monometer fluid
g - gravity constant
h - height of monometer fluid
h_{stag} - height for stagnation pressure of Pitot tube
h_{stat} - height for static pressure of Pitot tube
h_{atm} - height for room pressure
h_{tunnel} - height for tunnel static pressure

$$R = \frac{Q_{pitot}}{Q_{tunnel}} \tag{1}$$

$$Q_{pitot} = P_{stag} - P_{stat} \tag{2}$$

$$Q_{tunnel} = P_{atm} - P_{tunnel} \tag{3}$$

$$P = \rho g h \tag{4}$$

These pressures are converted into monometer oil heights using Equation 4. The fluid density and gravity constant are the same in all four pressures, so these constants cancel out to form Equation 5. The Data Reduction Equation for the wind tunnel correction factor eliminates the middle steps of dynamic pressure calculation. Equation 5 directly outputs the correction factor, with the only inputs being the measured fluid heights.

$$R = \frac{h_{stag} - h_{stat}}{h_{atm} - h_{tunnel}} \tag{5}$$

All of the measurements had a readability uncertainty of 0.1 inches because of the arrangement of tick marks on the manometer board. Using Equation 8, the systematic uncertainty was calculated to be 0.0150 inches for each of the samples.

$\omega_{R,total}$ - total uncertainty of *R*
$\omega_{R,syst}$ - systematic uncertainty in *R*
$\omega_{R,rand}$ - random uncertainty in *R*
$\omega_{h,stat}$ - uncertainty in h_{stat}
$\omega_{h,stag}$ - uncertainty in h_{stag}
$\omega_{h,atm}$ - uncertainty in h_{atm}
$\omega_{h,tunnel}$ - uncertainty in h_{tunnel}
t- *t*-value for *R*
S_R - standard deviation of *R*
n- number of trials

$$\omega_{R,total}^2 = \omega_{R,syst}^2 + \omega_{R,rand}^2 \tag{6}$$

$$\omega_{R,syst}^2 = \left(\frac{\partial R}{\partial h_{stat}}\right)^2 \omega_{h,stat}^2 + \left(\frac{\partial R}{\partial h_{stag}}\right)^2 \omega_{h,stag}^2 + \left(\frac{\partial R}{\partial h_{atm}}\right)^2 \omega_{h,atm}^2 + \left(\frac{\partial R}{\partial h_{tunnel}}\right)^2 \omega_{h,tunnel}^2 \tag{7}$$

$$\omega_{h,syst}^2 = \omega_{h,read}^2 + \omega_{h,acc}^2 \tag{8}$$

$$\omega_{R,rand}^2 = \frac{tS_R}{\sqrt{n}} \tag{9}$$

Results and Discussion

After 19 different trials recorded over the span of 3 days average wind tunnel correction factor was found to be 0.909 with an uncertainty of 0.018. Given our uncertainty range, this compares well to Dr. Mayhew's calculated correction factor of 0.941 from January 2011. This value was measured over two years ago, so the build-up of dust on the screen at the wind tunnel entrance could have depressed the wind tunnel correction factor over time. The recorded values for h_{stat}, h_{stag}, h_{tunnel}, and h_{atm} can be found in Appendix 1.

Using Equation 6, the total uncertainty for the average value of the correction factor was found to be 0.0177. The nature of our experimental apparatus does not produce a constant uncertainty. Instead, it produces a high relative uncertainty at lower wind speeds as shown in the Figure 4. On these figures, Delta H is $h_{tunnel} - h_{atm}$, this value is directly proportional to velocity.

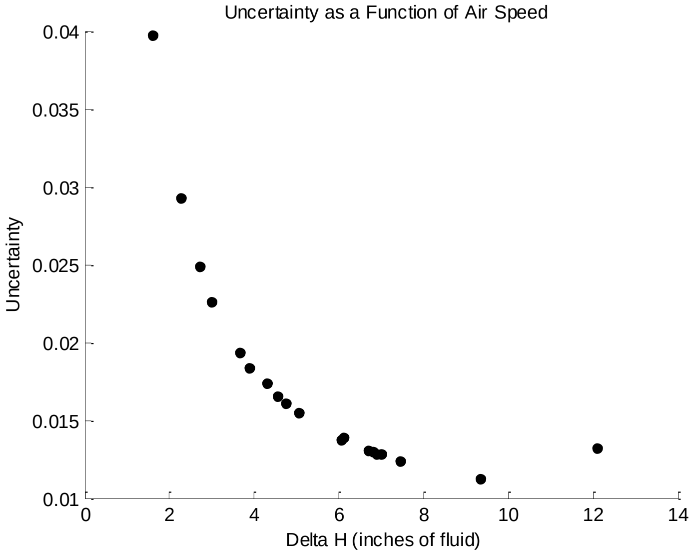

Figure 4: Correction factor uncertainty as a function of Delta H

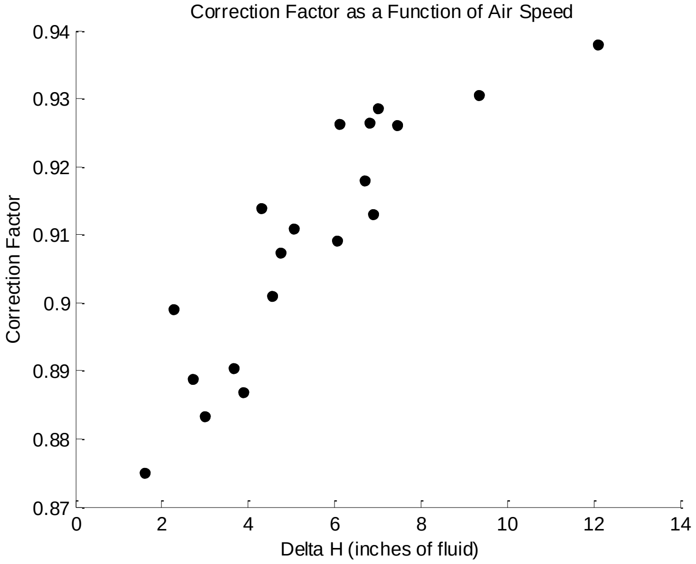

Figure 5: Correction factor as a function of Delta H

Conclusion

For wind tunnel 1 in the Rotz Lab, the average correction factor was found to be 0.909±0.018. As shown in Figure 5, there is a rough linear relationship between correction factor and the air speed because the correction factor increases with velocity. However, our data failed to definitively indicate a linear relationship, because the R^2 value of the linear fit is only 0.788. The uncertainties in correction factor increase significantly as the velocity decreases, as shown in Figure 4. This may have contributed to our poor linear fit. Therefore, we suggest using an average correction factor for a range of velocities instead of a linear relationship because of the nature of the uncertainty in the measurements taken with the manometer board. To get more accurate results, pressure transducers could be used in place of manometers to increase readability and resolution.

Appedix 1

Table 1: Experimental fluid height data

h_{stag}	h_{stat}	h_{tunnel}	h_{atm}
1.8	13.15	13.2	1.1
0.7	2.75	2.83	0.55
0.7	3.1	3.2	0.5
0.7	3.35	3.5	0.5
0.65	3.9	4.1	0.45
0.67	4.6	4.8	0.5
0.85	5.16	5.3	0.55
0.85	5.45	5.6	0.55
0.85	6.35	6.5	0.45
0.9	7.2	7.3	0.5
0.45	1.85	1.95	0.35
0.5	6.15	6.3	0.2
0.65	6.8	6.95	0.25
0.65	6.95	7.1	0.2
1.6	5.05	5.19	1.3
1.7	8.6	8.7	1.25
1.5	5.6	5.75	1.2
1.8	10.5	10.55	1.2
1.7	8.2	8.3	1.3